Shelf slope, estuarine dynamics and river plumes in a z* vertical coordinate, unstructured grid model

Giorgia Verri [a],[*], Ivano Barletta [a], Nadia Pinardi [b], Ivan Federico [a], Jacopo Alessandri [b], Giovanni Coppini [a]

[a] *Centro Euro-Mediterraneo sui Cambiamenti Climatici, CMCC, Lecce, Italy*
[b] *Department of Physics and Astronomy, University of Bologna, Bologna, Italy*

A B S T R A C T

The finite element, unstructured grid model SHYFEM has been used to carry out some fundamental studies on the quality of a specific type of Generalized Vertical Coordinate (GVC) system, the so-called z^* coordinates versus $z - geopotential$ coordinates. Idealized and realistic test cases are shown to assess the impact of the vertical coordinates on key physical processes, i.e. the internal tide generation at a continental slope, a river plume shape and intensity and the salt water intrusion.

The results showed that the z^* coordinates produce a stronger water column stratification than the $z - geopotential$ ones and together with the unstructured grid modeling they can better solve the coastal sea dynamics.

An idealized twin experiment configuration of the model was carried out to verify the proper implementation of the GVC z^* by simulating the production of internal tides at the continental slope. The results confirmed that the z^* coordinate model reproduces the expected internal tide fields better than $z - geopotential$ model. A set of realistic experiments in the Po river delta coastal region, demonstrated that the representation of the dynamical processes at the coastal scales is conditioned by the high resolution (25 cm layers), which was only possible by the z^* formulation in the upper water column.

1. Introduction

Choosing the right vertical coordinate system is key when designing a numerical ocean model, especially now that advanced ocean modeling uses regional configurations which include rivers, estuaries, shelves and part of the open sea (Federico et al., 2017; Park et al., 2022 among the others). The literature on ocean vertical coordinate system indicates two primary approaches to vertical discretization (Kasahara, 1974; Bleck, 1978a, 2002; Song and Haidvogel, 1994; Adcroft and Campin, 2004; Adcroft and Hallberg, 2006 among the others).

The first approach is the Eulerian $z - geopotential$, hereafter referenced simply as z, which discretizes the geometrical depth with respect to a bathymetry and all layers have a fixed thickness in time and space except for the top layer. This allows for a straightforward implementation. However, the free surface deviations from rest need to occur within the thickness of the first level. When tidal excursions are large, of the order of a few meters, this requires a thick surface layer thus producing a coarsely resolved upper ocean dynamics in the mixed layer.

The other vertical discretization approach is a Generalized Vertical Coordinate (GVC) system where layers thicknesses depend on time and space. Two GVC primary systems have been widely used: (i) the terrain following or σ coordinates (Phillips, 1957) and (ii) the *isopycnal* coordinates (Bleck et al., 1992; Oberhuber, 1993). The σ coordinates scale the time variable distance between the sea surface and the sea floor into discrete intervals, but with a constant number of levels throughout the computational domain. They offer a smooth and more realistic representation of the bottom topography and have been considered particularly useful for coastal modeling (Blumberg and Mellor, 1987). However, special care is needed to prevent errors in the horizontal pressure gradient term of the momentum equation when a highly stratified flow occurs along steep topography producing tilted and narrow layers (Stelling and Van Kester, 1994, Mellor et al., 1994, Mellor et al., 1998). The *isopycnal* coordinates base the vertical discretization on the density stratification thus the computational grid moves with the fluid and the water column is divided into layers of constant density and variable thickness. The dynamics are treated as Lagrangian in the vertical which makes them preferable for climate scale modeling (Griffies et al., 2000; Adcroft and Hallberg, 2006; Legg et al., 2009). This removes the spurious diapycnal mixing of the Eulerian coordinate systems (Ilicak et al., 2012 among the others).

---

* Corresponding author.
E-mail address: giorgia.verri@cmcc.it (G. Verri).

On the other hand, practical drawbacks include coarsely resolved upper ocean dynamics in the mixed layer and the potential layer degeneracy when the water column homogenizes (Bleck, 2002).

Recognizing that each of these coordinate systems has its advantages and disadvantages (as discussed in Griffies, 2004 and Klingbeil et al., 2018), efforts are underway to create a new generalized and hybrid coordinate approach, as in the new global ocean models (Ringler et al., 2013; Petersen et al., 2015; Forget et al., 2015; Danilov et al., 2017 among the others). They use the appropriate coordinates (i) at different depths, (ii) in different areas, and more recently (iii) at different frequencies (Leclair and Madec, 2011). In particular, the Arbitrary Lagrangian Eulerian (ALE) method (Bleck, 1978b, Adcroft and Hallberg, 2006) is gaining popularity as it allows the diabatic dynamics to be considered, in a pseudo-Lagrangian vertical coordinate system. With the ALE method, the equations are first integrated in a lagrangian system and then remapped to any arbitrary non-lagrangian coordinates (Bleck, 2002, Griffies et al., 2020) which allows for vertical cross-coordinate flow. The remapped vertical coordinates are chosen to match the fast motion thus dia-surface velocities are small and a relatively large time step is permitted even when smaller layer thicknesses and/or large vertical velocities occur (Griffies et al., 2020).

On the other hand, the new generation high resolution models solve a wide range of scales and processes by using the pressure method algorithm (Marshall et al., 1997) which cannot be used with a lagrangian treatment of the vertical coordinates (Adcroft and Hallberg, 2006).

Another line of research proposes to optimize the terrain-following coordinates by a local adjustment to virtual bottoms, also known as multi-envelope coordinates (Shapiro et al., 2013, Bruciaferri et al., 2018).

Here we focus on a specific GVC which is height-based but has advantages compared to z and σ coordinates, i.e. the z^* coordinates (Stacey et al., 1995) which evenly distribute the free surface oscillations in the local bathymetry depth, but without following the bottom topography as in σ case.

What make the z^* coordinates particularly suitable for cross-scale and multi-scale modeling purposes is the fact that they allow an extremely high resolution near the surface where buoyancy losses/gains occur thus inducing stratification changes. This is ensured not only in the shallow parts of the domain, as in the case of σ coordinates, but also in the open sea.

The z^* coordinates allow a multilayer representation of the shallow coastal regions including drying and flooding. Moreover the z^* moving layer interfaces reduce the numerical mixing of the advection schemes which may arise from high free surface oscillations in the fixed z-geopotential space; this is a crucial aspect for coastal to global models including tides (Klingbeil et al., 2018, Adcroft and Campin, 2004).

In addition the z^* coordinates are preferable to the σ ones which are prone to the aforementioned (i) horizontal pressure gradient error and (ii) coarse vertical resolution in the mixed layer where the local bathymetric depth increases.

For all the reasons discussed above, we chose z^* as the vertical coordinate system to be applied to a finite element unstructured grid model which was previously z-coordinate based. To our knowledge this is the first work that uses the z^* coordinates in an estuary and river plume with an unstructured grid model. Other studies have used the z^* coordinates with unstructured grid models covering the global ocean (Ringler et al., 2013; Petersen et al., 2015; Danilov et al., 2017; von Storch et al., 2023 as examples), but without assessing their performance for the estuarine dynamics and river plumes. Regional and coastal ocean models are currently mostly based on the terrain following coordinates, used within optimized or hybrid approaches (among them there are Zhang et al., 2015; Fofonova et al., 2021 using finite element codes and Bruciaferri et al., 2018; Polton et al., 2022; Wise et al., 2022 using finite difference codes). Wise et al. (2022) show that z^* might have limited accuracy for barotropic tides over the shelf with respect to terrain-following coordinates but it is demonstrated in

a tidal-only experiment, thus this is a question that could be considered in the future work. On the other hand, the z^* GVC allows a very fine discretization in the shallow coastal areas and the partial cells can be adapted to the bottom, thus preserving the representation of the bottom currents and the shelf to open sea exchange.

A further purpose of this study is to provide a detailed discussion the transformation of the "layer-integrated" governing equations and their vertical boundary conditions from the z to the z* coordinates space, because it differs from the well-known "level-discretized" GVC forms. The previous literature provided a comprehensive treatment of the GVC transformation for the continuous form of the governing equations (Kasahara, 1974; Burchard and Petersen, 1997, Adcroft and Campin, 2004 among others) which can be easily adapted to the "level-discretized" case with no changes while the "layer-integrated" governing equations have some peculiarities and different expressions (as explained by Burchard and Petersen, 1997) that deserve to be detailed.

We start with the System for HYdrodynamic Finite Element Modules, SHYFEM, which is an open source finite element ocean circulation model (https://github.com/SHYFEM-model/shyfem) previously described in Umgiesser et al. (2004), Bellafiore and Umgiesser (2010), Maicu et al. (2021) and Micaletto et al. (2021). SHYFEM discretizes the spatial domain by means of staggered finite elements, i.e. using an Arakawa B grid, with an adaptive spacing based on the Delaunay triangulation which leads to smoothly varying mesh transitions from larger to coastal scales. The vertical discretization is based on $z - geopotential$ coordinates with "partial cells" at the bottom (Adcroft et al., 1997), i.e. the bottom interfaces are adjusted at the start time to closely follow the realistic bathymetry.

Two experiments are discussed: (i) an idealized experiment representing the internal tide generation by a topographic slope; (ii) a realistic experiment with a high resolution coastal configuration which includes a river delta system and the shelf sea adjacent to the river mouths. The experiments compare the z and z^* formulations and prove the advantages of the latter.

The paper is organized as follows. Section 2 presents the transformation of the governing equations in the z^* coordinate system. Sections 3 and 4 introduce the idealized and realistic experiments to assess the model behavior and skills, respectively. Concluding remarks and the future perspectives are given in Section 5.

2. The transformation of SHYFEM layer integrated primitive equations into the GVC system

We discuss the transformation of the "layer-integrated" governing equations from the z coordinates to z^* because it gives different expressions from the "level-discretized" GVC form, which is reported for comparison in Appendix. In this way we complete the literature formalism for such a transformation.

2.1. The layer-integrated primitive equations in the z coordinates

The physical core of SHYFEM consists of eight hydrodynamical and thermodynamical equations with the Boussinesq and hydrostatic approximations. The model uses a layer-integrated equation form where the dynamical variables are considered to be constant in the layers. This means that for the horizontal velocity components $\vec{u} = (u, v)$ in a layer limited by the interfaces z_{i-1} and z_i we have:

$$\int_{z_i}^{z_{i-1}} \vec{u}_i dz = (z_{i-1} - z_i)\vec{u}_i = \vec{U}_i \tag{1}$$

Similarly the layer integrated tracers θ and S read as follow:

$$\int_{z_i}^{z_{i-1}} S_i dz = (z_{i-1} - z_i)S_i = H_i S_i \tag{2}$$

Table 1
List of variables and parameters used in the SHYFEM z and z^* governing equations.

Symbol	Name	Notes
z_i , z_i^*	Location of bottom interface of layer i	Units of m
U_i, V_i	Zonal and meridional transports of layer i	Units of m^2s^{-1}
u_i, v_i	Zonal and meridional velocities of layer i	$u_i = \frac{U_i}{H_i}$, $v_i = \frac{V_i}{H_i}$ Units of ms^{-1}
w_i	Vertical velocity across z-bottom surface of layer i	Units of ms^{-1}
w_i^*	Dia-surface velocity across z^*-bottom surface of layer i	Units of ms^{-1}
$\hat{U}$, $\hat{V}$	Zonal and meridional barotropic transports	$\hat{U} = \sum U_i$, $\hat{V} = \sum V_i$ Units of m^2s^{-1}
H_i	Thickness of layer i	See formula (29) Units of m
η	Non linear free surface elevation	Units of m
p_{atm}	Atmospheric pressure at the sea surface	Units of $\text{kgm}^{-1}\text{s}^{-2}$
ρ_0	Reference density at the sea surface	Units of kgm^{-3}
ρ_i'	Density oscillation of layer i	Units of kgm^{-3}
ρ_i	Total density of layer i	$\rho_i = \rho_0 + \rho_i'$ Units of kgm^{-3}
S_i	Salinity of layer i	Units of psu
θ_i	Potential temperature of layer i	Units of $^\circ\text{K}$
p_i	Hydrostatic pressure of layer i	Units of $\text{kgm}^{-1}s^{-2}$
τ_{xz}^i, τ_{yz}^i	Turbulent shear stresses in xz and yz plane	Units of m^2s^{-2}
A_H, A_V	Horizontal and vertical eddy viscosity coefficients	Units of m^2s^{-1}
K_H, K_V	Horizontal and vertical eddy diffusivity coefficients	Units of m^2s^{-1}
ν, γ	Molecular viscosity and diffusivity coefficients	Units of m^2s^{-1}
E, P	Evaporation and Precipitation rate	Units of ms^{-1}
I	Heat flux transmitted by radiative processes through water column	See formula (16) Units of $\text{Js}^{-1}\text{m}^{-2}$
T_r	Percentage of entering radiation depending on the Jerlov classification of water type (Jerlov, 1976)	see formula (16) dimensionless
λ_1 and λ_2	Two length scales of solar penetration	See formula (16)
f	Coriolis parameter	Units of s^{-1}

$$\int_{z_i}^{z_{i-1}} \theta_i dz = (z_{i-1} - z_i)\theta_i = H_i \theta_i \tag{3}$$

All the symbols are explained in Table 1.

The primitive equations integrated over layer i in the z space are listed below following the order in which they are solved by the code:

$$\frac{\partial U_i}{\partial t} + u_i\frac{\partial U_i}{\partial x} + v_i\frac{\partial U_i}{\partial y} + \int_{z_i}^{z_{i-1}} w\frac{\partial u}{\partial z}dz = -\frac{H_i}{\rho_0}\frac{\partial p_{atm}}{\partial x} - gH_i\frac{\partial \eta}{\partial x} +$$
$$-g\frac{H_i}{\rho_0}\int_{z_{i_{mid}}}^{\eta}\frac{\partial \rho'}{\partial x}dz + \int_{z_i}^{z_{i-1}}\frac{\partial \tau_{xz}}{\partial z}dz + H_iA_H\nabla_h^2 u_i + H_i\nu\nabla^2 u_i + fV_i \tag{4}$$

$$\frac{\partial V_i}{\partial t} + u_i\frac{\partial V_i}{\partial x} + v_i\frac{\partial V_i}{\partial y} + \int_{z_i}^{z_{i-1}} w\frac{\partial v}{\partial z}dz = -\frac{H_i}{\rho_0}\frac{\partial p_{atm}}{\partial y} - gH_i\frac{\partial \eta}{\partial y} +$$
$$-g\frac{H_i}{\rho_0}\int_{z_{i_{mid}}}^{\eta}\frac{\partial \rho'}{\partial y}dz + \int_{z_i}^{z_{i-1}}\frac{\partial \tau_{yz}}{\partial z}dz + H_iA_H\nabla_h^2 v_i + H_i\nu\nabla^2 v_i - fU_i \tag{5}$$

$$\frac{\partial \eta}{\partial t} + \frac{\partial}{\partial x}\hat{U} + \frac{\partial}{\partial y}\hat{V} = P - E \tag{6}$$

$$w_i - w_{i-1} = \frac{\partial U_i}{\partial x} + \frac{\partial V_i}{\partial y} \tag{7}$$

$$\frac{\partial(H_iS_i)}{\partial t} + \frac{\partial(U_iS_i)}{\partial x} + \frac{\partial(V_iS_i)}{\partial y} + \int_{z_i}^{z_{i-1}}\frac{\partial wS}{\partial z}dz = H_iK_H\nabla_h^2 S_i$$
$$+ \int_{z_i}^{z_{i-1}}\frac{\partial}{\partial z}K_V\frac{\partial S}{\partial z}dz + H_i\gamma\nabla^2 S_i \tag{8}$$

$$\frac{\partial(H_i\theta_i)}{\partial t} + \frac{\partial(U_i\theta_i)}{\partial x} + \frac{\partial(V_i\theta_i)}{\partial y} + \int_{z_i}^{z_{i-1}}\frac{\partial w\theta}{\partial z}dz = H_iK_H\nabla_h^2\theta_i$$
$$+ \int_{z_i}^{z_{i-1}}\frac{\partial}{\partial z}K_V\frac{\partial \theta}{\partial z}dz +$$
$$+ H_i\gamma\nabla^2\theta_i + \frac{1}{\rho C_p}\int_{z_i}^{z_{i-1}}\frac{\partial I}{\partial z}dz \tag{9}$$

$$p_i(x,y,z_{i_{mid}},t) = \rho_0\,g(\eta - z_{i_{mid}}) + \int_{z_{i_{mid}}}^{\eta}\rho' g\,dz \tag{10}$$

$$\rho_i(x,y,z_{i_{mid}},t) = \rho_i(S_i, \theta_i, p_i) \tag{11}$$

where (x, y, z_i, t) are the horizontal, vertical and time coordinates, i=1, ..N is the vertical layer index, z_i is the depth of the bottom interface of layer i and $z_{i_{mid}}$ is the depth at middle of layer i. The Eqs. (4)–(5)–(6)–(8)–(9) are the prognostic equations for the horizontal transport in the zonal $U_i(x, y, z_i, t)$ and meridional $V_i(x, y, z_i, t)$ directions, the sea surface height $\eta(x, y, t)$ where $(\hat{U}, \hat{V})$ is the barotropic transport, $S_i(x, y, z_i, t)$ is the practical salinity and $\theta_i(x, y, z_i, t)$ is the potential temperature. The Eq. (7) is the vertically integrated continuity equation for the computation of the vertical velocity $w_i(x, y, z_i, t)$. The Eq. (10) is the layer-integrated hydrostatic equation for pressure $p_i(x, y, z_{i_{mid}}, t)$. The equation of state (11) is the Unesco equation of state (Fofonoff and Millard, 1983) and provides the total density which is the sum of the reference density at the sea surface plus the density oscillations of layer i: $\rho_i(x, y, z_i, t) = \rho_0 + \rho'(x, y, z_i, t)$.

The layer integral of the stress terms of Eqs. (4)–(5) are computed as follows:

$$\int_{z_i}^{z_{i-1}}\frac{\partial \tau_{xz}}{\partial z}dz = \tau_{xz}^{i-1} - \tau_{xz}^i = A_V\frac{\partial u}{\partial z}\bigg|_{i-1} - A_V\frac{\partial u}{\partial z}\bigg|_i \tag{12}$$

$$\int_{z_i}^{z_{i-1}}\frac{\partial \tau_{yz}}{\partial z}dz = \tau_{yz}^{i-1} - \tau_{yz}^i = A_V\frac{\partial v}{\partial z}\bigg|_{i-1} - A_V\frac{\partial v}{\partial z}\bigg|_i \tag{13}$$

where the turbulent shear stresses τ_{xz}^i and τ_{yz}^i are defined at the bottom interface of each layer and are written according to the flux-gradient theory with the vertical eddy viscosity coefficients A_V solved through a second order closure schemes (based on the GOTM model (Burchard et al. 1999)). The turbulent shear stresses at the free surface, τ_{xz}^0 and τ_{yz}^0, and at the bottom, τ_{xz}^N and τ_{yz}^N are defined by the momentum surface and bottom boundary conditions listed hereafter. The turbulent diffusive terms in Eqs. (8)–(9) are computed as follows:

$$\int_{z_i}^{z_{i-1}}\frac{\partial}{\partial z}K_V\frac{\partial \theta}{\partial z}dz = K_V\frac{\partial \theta}{\partial z}\bigg|_{i-1} - K_V\frac{\partial \theta}{\partial z}\bigg|_i \tag{14}$$

$$\int_{z_i}^{z_{i-1}}\frac{\partial}{\partial z}K_V\frac{\partial S}{\partial z}dz = K_V\frac{\partial S}{\partial z}\bigg|_{i-1} - K_V\frac{\partial S}{\partial z}\bigg|_i \tag{15}$$

$\tau_{Sz}^i = K_V\frac{\partial S}{\partial z}$ and $\tau_{\theta z}^i = K_V\frac{\partial \theta}{\partial z}$ are defined at the bottom interface of each layer according to the flux-gradient theory with the vertical eddy diffusivity coefficients K_V computed by the same second order closure scheme as for A_V. The last term on the RHS of Eq. (9) includes the specific heat capacity of seawater C_p (units of J/kg $*$ $^\circ$K) and the solar irradiance I_i representing the heat flux transmitted through the water column up to depth z_i (units of $\text{Js}^{-1}\text{m}^{-2}$) and given by:

$$I_i = I(z_i) = Q_s\left(T_r e^{\frac{z_i-\eta}{\lambda_1}} + (1 - T_r)e^{\frac{z_i-\eta}{\lambda_2}}\right) \tag{16}$$

where Q_s represents the net downward solar irradiance at the sea surface and all the other symbols are explained in Table 1. Note that at the free surface interface $I(\eta) = Q_s$.

The surface boundary conditions for the momentum flux, the diffusive heat and salt fluxes and the vertical velocity are specified at the sea surface $z = \eta$ as follows:

$$A_V \frac{\partial \vec{u}}{\partial z}\bigg|_{z=\eta} = \frac{\rho_a}{\rho_0} C_D |\vec{u}_w| \vec{u}_w \tag{17}$$

$$K_V \frac{\partial \theta}{\partial z}\bigg|_{z=\eta} = \theta(\eta)(E - P) - \frac{Q_{net}}{\rho_o C_p} \tag{18}$$

$$K_V \frac{\partial S}{\partial z}\bigg|_{z=\eta} = S(\eta)(E - P) \tag{19}$$

$$w\bigg|_{z=\eta} = \frac{D\eta}{Dt} + (E - P) \tag{20}$$

where ρ_a is the air density, $\vec{u}_w = (u_w, v_w)$ are the wind velocity components near the sea surface, and C_D is the wind drag coefficient following (Hellerman and Rosenstein, 1983), Q_{net} is the net downward heat flux and C_p coefficient is the specific heat of the sea water.

The bottom boundary conditions at the sea floor depth $z = -H_{B_{floor}}$ are:

$$A_V \frac{\partial \vec{u}}{\partial z}\bigg|_{z=-H_{B_{floor}}} = \frac{C_B}{H_N^2} |\vec{U}_N| \vec{U}_N \tag{21}$$

$$K_V \frac{\partial \theta}{\partial z}\bigg|_{z=-H_{B_{floor}}} = 0 \tag{22}$$

$$K_V \frac{\partial S}{\partial z}\bigg|_{z=-H_{B_{floor}}} = 0 \tag{23}$$

$$w\bigg|_{z=-H_{B_{floor}}} = 0 \tag{24}$$

where $\vec{U}_N = (U_N, V_N)$ are the horizontal transport components at the bottom layer, H_N is the thickness of the bottom layer $i = N$ and C_B is the dimensionless bottom drag coefficient defined as logarithmic function fo the bottom roughness length λ_B and the water column depth as follows:

$$C_B = \left(\frac{0.4}{ln(\frac{\lambda_B + 0.5(H_{B_{floor}} + \eta)}{\lambda_B})} \right)^2$$

Details on the time-discretization (i.e. explicit, semi-implicit and fully implicit time stepping are allowed depending on the physical processes), the numerical schemes and the parameterizations can be found in Umgiesser et al. (2004), Bellafiore and Umgiesser (2010) and Micaletto et al. (2021).

2.2. Transforming the layer-integrated primitive equations in the z^* coordinates

Following Stacey et al. (1995), the rescaled and time-dependent z^* vertical coordinate is defined as follows:

$$z^*(x, y, z, t) = \frac{z - \eta(x, y, t)}{H_{B_{floor}}(x, y) + \eta(x, y, t)} H_{B_{floor}}(x, y) \tag{25}$$

Top panels of Fig. 1 show the transformation of the z coordinate system into the z^* space according to the definition (25). Thus $z^*(z = \eta) = 0$ and $z^*(z = -H_{B_{floor}}) = -H_{B_{floor}}$.

In this new vertical coordinate system, the integrals ((1), (2), (3)) become:

$$\int_{z_i^*}^{z_{i-1}^*} \vec{u}_i \frac{\partial z}{\partial z^*} dz^* = \frac{H_{B_{floor}} + \eta}{H_{B_{floor}}} (z_{i-1}^* - z_i^*) \vec{u}_i \tag{26}$$

$$\int_{z_i^*}^{z_{i-1}^*} S_i \frac{\partial z}{\partial z^*} dz^* = \frac{H_{B_{floor}} + \eta}{H_{B_{floor}}} (z_{i-1}^* - z_i^*) S_i \tag{27}$$

$$\int_{z_i^*}^{z_{i-1}^*} \theta_i \frac{\partial z}{\partial z^*} dz^* = \frac{H_{B_{floor}} + \eta}{H_{B_{floor}}} (z_{i-1}^* - z_i^*) \theta_i \tag{28}$$

where $\frac{\partial z}{\partial z^*} = \frac{H_{B_{floor}} + \eta}{H_{B_{floor}}}$ is the Jacobian of the transformation.

We introduce the ith time-dependent layer thickness, $H_i(x, y, t)$ as follows:

$$H_i\bigg|_{t>0} = \frac{H_{B_{floor}} + \eta}{H_{B_{floor}}} (z_{i-1}^* - z_i^*)_{t=0} \tag{29}$$

Bottom panels of Fig. 1 show the discretization of the water column thickness into the z^* layers with respect to the case of z-geopotential layers, as defined in (29).

A new definition of vertical velocity is the dia-surface velocity w^*, which represents the vertical velocity across constant-z^* surfaces in the Eulerian z-space, thus it is written as the material derivative of z^* and reads as below:

$$w^* = \frac{Dz^*}{Dt}\bigg|_z = \frac{\partial z^*}{\partial t} + u \frac{\partial z^*}{\partial x} + v \frac{\partial z^*}{\partial y} + w \frac{\partial z^*}{\partial z} \tag{30}$$

To derive the layer-integrated equations in the z^* space, first we transform the z level-discretized equations into the z^* space (Eqs. (43)–(50) in the Appendix) and then we integrate over the i layer thickness by applying the definitions (26)–(29).

The new set of z^* layer-integrated equations is listed below in the same order of the original z coordinate ones, (4)–(11).

$$\frac{\partial U_i}{\partial t} + u_i \frac{\partial U_i}{\partial x} + v_i \frac{\partial U_i}{\partial y} + \int_{z_i^*}^{z_{i-1}^*} \overline{w} \frac{\partial u}{\partial z^*} dz^* = -\frac{H_i}{\rho_0} \frac{\partial p_{atm}}{\partial x} - g H_i \frac{\partial \eta}{\partial x} +$$
$$-g \frac{H_i}{\rho_0} \int_{z_{i_{mid}}^*}^{0} \frac{\partial z}{\partial z^*} \left(\frac{\partial \rho'}{\partial x} - \frac{\partial \rho'}{\partial z} \frac{\partial z_i}{\partial x} \right) dz^* + (\tau_{xz}^{i-1} - \tau_{xz}^i)$$
$$+ H_i A_H \nabla_h^2 u_i + H_i \nu \nabla^2 u_i + f V_i \tag{31}$$

$$\frac{\partial V_i}{\partial t} + u_i \frac{\partial V_i}{\partial x} + v_i \frac{\partial V_i}{\partial y} + \int_{z_i^*}^{z_{i-1}^*} \overline{w} \frac{\partial v}{\partial z^*} dz^* = -\frac{H_i}{\rho_0} \frac{\partial p_{atm}}{\partial y} - g H_i \frac{\partial \eta}{\partial y} +$$
$$-g \frac{H_i}{\rho_0} \int_{z_{i_{mid}}^*}^{0} \frac{\partial z}{\partial z^*} \left(\frac{\partial \rho'}{\partial y} - \frac{\partial \rho'}{\partial z} \frac{\partial z_i}{\partial y} \right) dz^* + (\tau_{yz}^{i-1} - \tau_{yz}^i)$$
$$+ H_i A_H \nabla_h^2 v_i + H_i \nu \nabla^2 v_i - f U_i \tag{32}$$

$$\frac{\partial \eta}{\partial t} + \frac{\partial}{\partial x} \hat{U} + \frac{\partial}{\partial y} \hat{V} = P - E \tag{33}$$

$$\overline{w}_i - \overline{w}_{i-1} = \frac{\partial}{\partial t} H_i + \frac{\partial U_i}{\partial x} + \frac{\partial V_i}{\partial y} \tag{34}$$

$$\frac{\partial(H_i S_i)}{\partial t} + \frac{\partial(U_i S_i)}{\partial x} + \frac{\partial(V_i S_i)}{\partial y} + \int_{z_i^*}^{z_{i-1}^*} \frac{\partial(\overline{w} S)}{\partial z^*} dz^* = H_i K_H \nabla_h^2 S_i$$
$$+ \int_{z_i^*}^{z_{i-1}^*} \frac{\partial}{\partial z^*} K_V \frac{\partial S}{\partial z^*} dz^* + H_i \gamma \nabla^2 S_i \tag{35}$$

$$\frac{\partial(H_i \theta_i)}{\partial t} + \frac{\partial(U_i \theta_i)}{\partial x} + \frac{\partial(V_i \theta_i)}{\partial y} + \int_{z_i^*}^{z_{i-1}^*} \frac{\partial(\overline{w} \theta)}{\partial z^*} dz^* = H_i K_H \nabla_h^2 \theta_i$$
$$+ \int_{z_i^*}^{z_{i-1}^*} \frac{\partial}{\partial z^*} K_V \frac{\partial \theta}{\partial z^*} dz^* +$$
$$+ H_i \gamma \nabla^2 \theta_i + \frac{1}{\rho C_p} \int_{z_i^*}^{z_{i-1}^*} \frac{\partial I}{\partial z^*} dz^* \tag{36}$$

$$p_i = \rho_0 \, g |z_{i_{mid}}^*| + \int_{z_{i_{mid}}^*}^{0} \frac{\partial z}{\partial z^*} \rho' g \, dz^* \tag{37}$$

$$\rho_i(x, y, z_{i_{mid}}^*, t) = \rho_i(S_i, \theta_i, p_i) \tag{38}$$

where the velocity $\overline{w}$ (Burchard and Petersen, 1997) is linked to the dia-surface velocity w^* as:

$$\overline{w} = \frac{\partial z}{\partial z^*} \left(w^* - u \frac{\partial z^*}{\partial x}\bigg|_z - v \frac{\partial z^*}{\partial y}\bigg|_{z^*} \right) \tag{39}$$
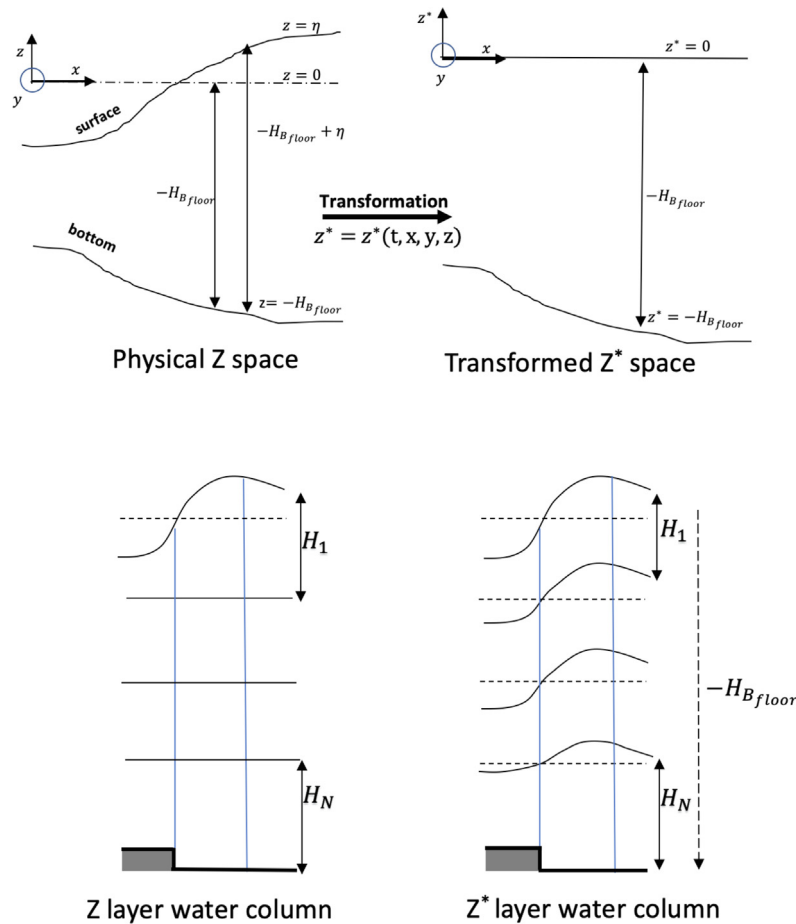
Fig. 1. Comparison between the vertical coordinates z and z^*. Top panel: sketch of the vertical coordinate transformation into the z^* space (adapted from Burchard and Petersen, 1997). Bottom panel: sketch of the discretization of the water column thickness in the z and z^* layers.

By comparing the z^* layer integrated Eqs. (31)–(38) with the ones in the z coordinate (4)–(11), two additional terms are revealed by the transformation into the GVC space: (i) a "tendency term" in the continuity equation (i.e. the first term on the right hand side of Eq. (34)), (ii) an additional expression in the baroclinic pressure gradient term, i.e. the third term in the right hand side of Eqs. (31)–(32). The z^* layer integrated Eqs. (31)–(38) do not contain the Jacobian of the coordinate transformation in any of the terms of the momentum, tracer and continuity equations, unlike in the level-discretized Eqs. (43)–(50) provided in the Appendix. This is the result of applying the definitions (26)–(29) as demonstrated in Burchard and Petersen (1997).

The baroclinic pressure gradient term is written with the horizontal derivative computed before the vertical integral in both the z and z^* equations (while in most z-coordinate models the two operations are in the reverse order). In fact, this is the form of the baroclinic pressure gradient term when the "density Jacobian method" is applied and this is the most suitable approach in a GVC space (Shchepetkin and McWilliams, 2003).

The surface boundary conditions in the z^* coordinate are the same as written in (17)–(20) except for the kinematic boundary condition at the free surface (20) which becomes as demonstrated by (Adcroft and Campin, 2004):

$$w^*(z^* = 0) = -\frac{H}{H + \eta}(P - E) \tag{40}$$

The bottom boundary conditions in the z^* coordinate do not change with respect to (21)–(24).

3. Idealized internal tide experiment

The idealized experiments are a rigorous way to start the evaluation of a numerical model development as they consist of simplified set-ups and mean that processes can be assessed individually thus highlighting the model's strengths.

Here we assess the capability of the previous z and the new developed z^* models to represent the internal wave generation due to the interaction of the barotropic tides with a continental slope.

We follow the setting up of the idealized experiment proposed by Adcroft and Campin (2004) where a structured, finite difference grid model was used. To our knowledge this experiment has not been repeated for finite element, unstructured grid models. The simplified ocean basin is 18 km long in the along-shelf direction, as shown in Fig. 2, and 5 km wide in the cross-shelf direction (not shown). The maximum depth is 200 m in the deepest part of the domain and it connects to a continental shelf 40 m deep with a linear shelf slope, and a uniform vertical resolution of 10 m. The domain has one open boundary on the offshore side and a closed one at the shelf side. A barotropic sinusoidal flow is prescribed at the open boundary with 12-hour period and 2 m amplitude thus resembling a barotropic tide impinging on the slope. The test case uses a linear equation of state of the form:

$$\rho = \rho_N[1 - \alpha(T - T_B)] \tag{41}$$

where $\rho_N = 1028$ kgm^{-3} is the reference density of sea water at the bottom, $\alpha = 2 * 10^{-4}$ °C^{-1} is the thermal expansion coefficient, $T_B = 5$ °C is the initial temperature at the bottom. The model is initialized
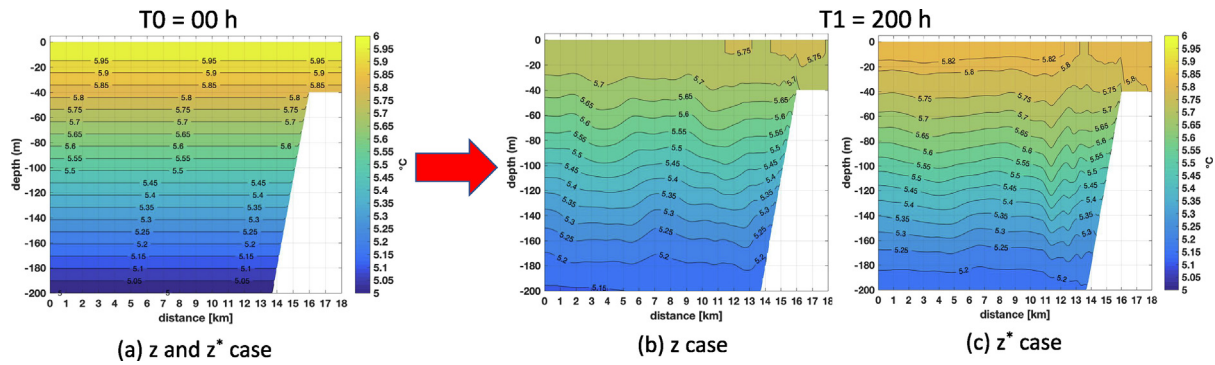
Fig. 2. Internal tide test case: Temperature field along the topography slope with SHYFEM z and z^* models. Panel (a) refers to the start time, panels (b) and (c) show the fields after 200 h for z and z^* models, respectively.
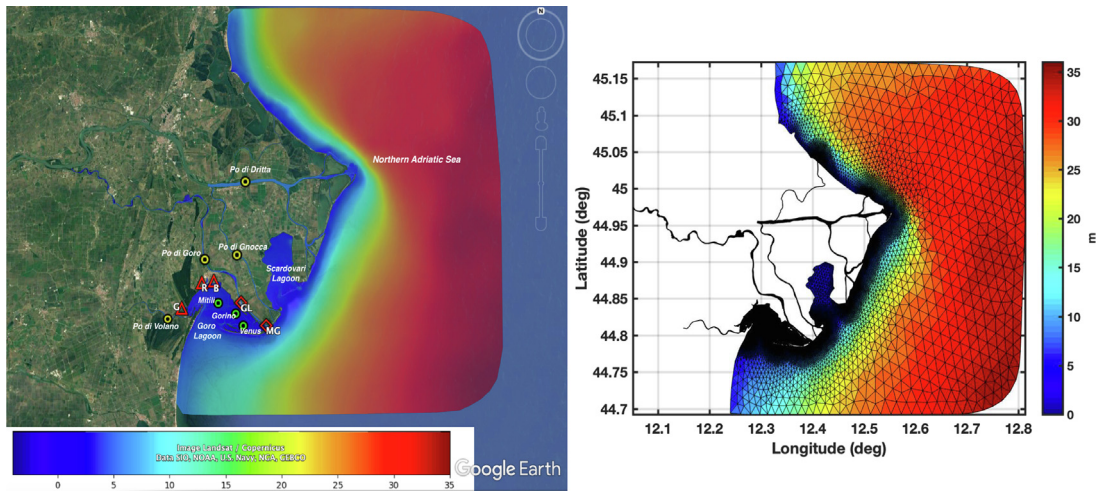

Fig. 3. Left panel: Realistic test case domain and bathymetry. The green circles are the CTD stations used for validation (Gorino, Mitili and Venus) . The yellow circles identify the freshwater branches. The red triangles are the pumping stations: Giralda (G), Romanina (R) and Bonello (B). The red diamonds are the connections of the Goro lagoon with the Po di Goro branch: the Gorino lock (GL) and the Manufatto gate (MG). Right panel: the finite element adaptive mesh.

at rest with a uniform stratification such that:

$$T(z) = T_B + \frac{T_T - T_B}{z_B - z_T}(z_B - z) \tag{42}$$

with the initial difference between top and bottom $T_T - T_B = 1\ °C$ and $z_T = 5$ m and $z_B = 200$ m. The along-shelf section of temperature at the initial state is show in the left panel of Fig. 2.

A twin experiment was performed using SHYFEM z and z^* GVC.

First, the time varying and fine stratification of the water column is captured by the z^* coordinates, as evident in the rightmost panel in Fig. 2, because they follow the barotropic flow prescribed at the open boundary by moving with the free surface oscillations. On the other hand, the z coordinate system is fixed.

After about 200 h (middle and right panels in Fig. 2), the z^* code is able to represent the internal wave generation, with the barotropic tide reflected on the continental shelf in the downslope and offshore direction, while the z code fails.

As explained by Adcroft and Campin (2004): the constriction presented to the horizontal flow by the continental slope leads to a relative acceleration of flow over the slope and shelf. During the on-shore phase of the tidal forcing, deep water is advected up the continental slope leading to a lateral buoyancy anomaly. The strength of upwelling anomalies on the slope is stronger in the z^* model, leading to well-defined internal waves emanating from the slope during the off-shore phase.

The different stratification observed between the twin experiments by using the same number of vertical levels could be even higher because the z^* coordinates allow an extremely fine discretization of

the first few meters at the top of the water column, irrespectively of the tidal range. We exploit this z^* capability in the realistic experiment we propose in the next section.

Overall, the twin idealized experiment proves the correct implementation of the GVC z^* and indicates that z^* is a more natural coordinate than z for modeling the interaction of the barotropic tides with the ocean stratification and bathymetry.E

4. Realistic experiment

A realistic experiment was carried out over a spatial domain covering the delta system of the Po river and a partial part of its region of freshwater influence, i.e. the shelf up to 20 km offshore the delta (Maicu et al., 2021) in the Northern Adriatic sub-basin. Fig. 3 shows the bathymetry of the selected area (left panel) and the finite element mesh (right panel). The final bathymetry considered in the model setup is obtained by merging the EMODnet data at 250 m resolution in the open sea area with the recent coastal multi-beam surveys operated by Arpae (Emilia Romagna regional Environmental Agency).

The experimental configuration of the SHYFEM z model for this case study is based on the implementation described in Maicu et al. (2021). Horizontal resolution is variable over the domain and spans from 2.2 km at the open boundary to less than 10 m along the branches of the delta system and inside the Scardovari and Goro lagoons, with a total number of 77 496 elements. Overall the study site is a shallow area with a maximum depth of 34.6 m and a low tidal range of about 1 m in the shelf sea facing the delta.

Table 2
Details of model setup.

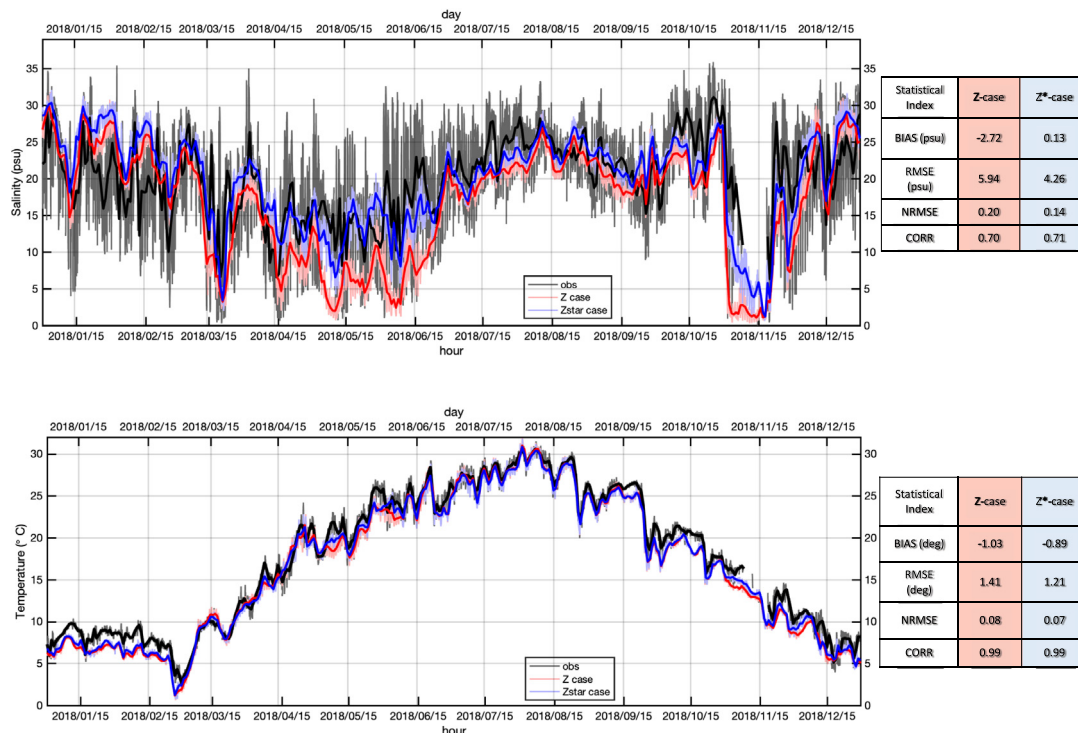| Name	Model vertical coordinates	Vertical layers
EXP0	z	10 layers with 1 m thicknesses in the top of the water column and other 7 layers below with increasing thickness up to 5 m at the bottom layer
EXP1	z*	17 layers as in EXP0
EXP2	z*	20 layers, with 4 layersof 25 cm each in the first water column meter

Fig. 4. Time series of simulated and observed salinity (top panel) and temperature (bottom panel) at Venus CTD station. Shaded lines are at hourly frequency and firm lines are daily averages. The inset tables show the statistics for the z model in EXP0 and EXP2 with z^*: RMSE, BIAS, NRMSE and Pearson correlation coefficient CORR.

The freshwater sources are imposed at the entrance of the Po in the domain, at the upstream of the artificial channel called Po di Volano and of the three pumping stations along the Po di Goro lagoon because they are regulated (shown in Fig. 3). At these locations, monthly climatological temperature based on data collected by ArpaE and zero salinity values are prescribed. Daily observed discharge is provided at the river open boundaries.

We performed three experiments from December 1st 2017 to December 31th 2018 that are described in Table 2. EXP0 is a 17 z layers experiment with 10 layers with ten 1 m thick layers at the top of the water column, and the other seven layers below with increasing thicknesses up to 5 m in the bottom layer. During the simulated time window, the oscillations of the free surface in the computational domain never exceed 80 cm around the zero line thus the z model could only use the 1 m top level. EXP1 uses the same layer distribution of EXP0 but with z^* for intercomparison. EXP2 uses 20 z^*-layers replacing the 1 m deep top layer with 4 layers with a thickness of 25 cm as allowed by this coordinate system.

The atmospheric forcing used to compute the surface boundary conditions come from the COSMO-I2 model analyses, with 2.8 km as horizontal resolution and 1 h frequency (Steppeler et al., 2003). The initial and the offshore lateral boundary conditions on temperature, salinity, velocity and sea surface height are imposed from the analyses of the Adriatic Sea sub-regional basin model AdriaROMS (Chiggiato and Paolo, 2008; Russo et al., 2013) with 2 km resolution in the Northern Adriatic. The eight main tidal components of the sea surface height are derived from the Oregon State University (OSU) TPXO

model (Egbert and Erofeeva, 2002) and added to the sea surface height lateral boundary condition. Further details on the numerical set-up are in Maicu et al. (2021).

In the following we validate the three experiments with observational data. We then show some of the key physical structures emerging from processes that characterize the estuarine dynamics in the EXP0 and EXP2 cases: i.e. the river plume shape and intensity in the shelf area, the estuarine water exchange and the salt wedge intrusion along the Po di Goro branch and the estuarine circulation in the Goro lagoon.

4.1. Validation with observations

We quantify the model performance using a comparison with three CTD buoys located in the Goro lagoon. The three stations (Mitili, Gorino and Venus stations shown in the left panel in Fig. 3) provide the near surface salinity and temperature with hourly frequencies. The Figs. 4–5–6 show the modeled and observed salinity and temperature during the simulation period, with December 2017 as the spin-up period. Since EXP0 and EXP1 gave very similar results, only the comparison between EXP0 and EXP2 are shown.

The quantitative comparison for temperature at all stations highlights that z^* is closer to observations with a 10%–20% smaller value in the NRMSE score, a decreased RMSE and bias. As discussed in Maicu et al. (2021), for salinity the accuracy is connected to the fresh water inputs more than the numerical scheme used. The salinity bias and RMSE are considerably reduced in z^* at the Venus station which is the furthest away from the Po river and channel mouths. For the other two
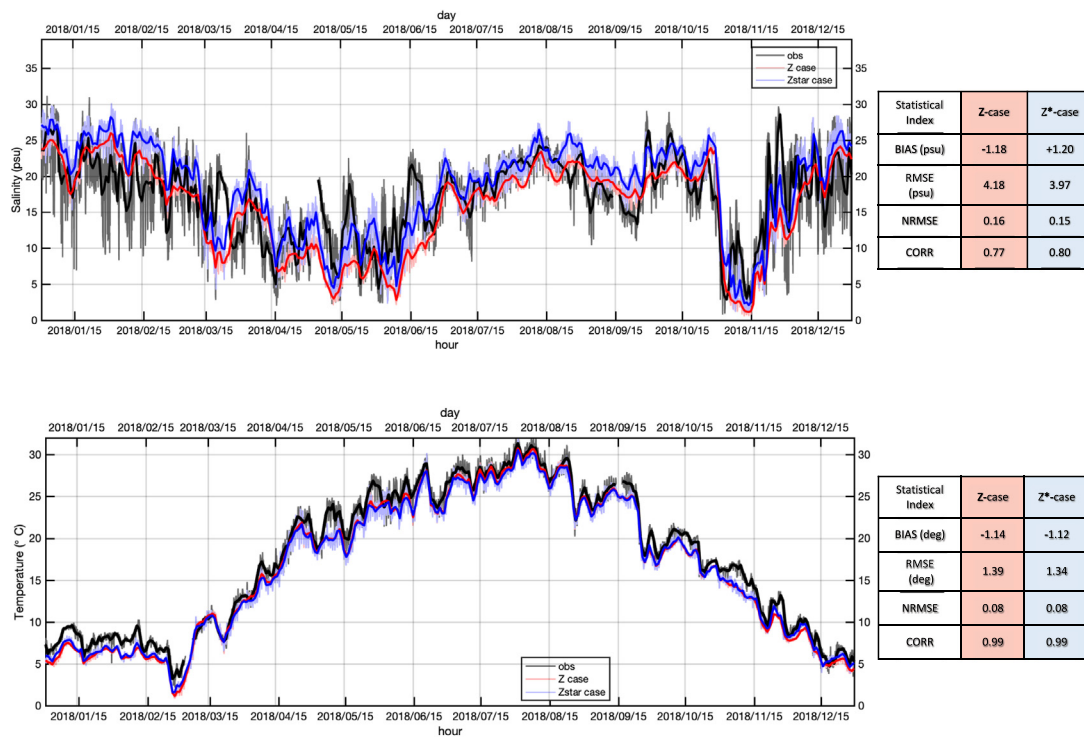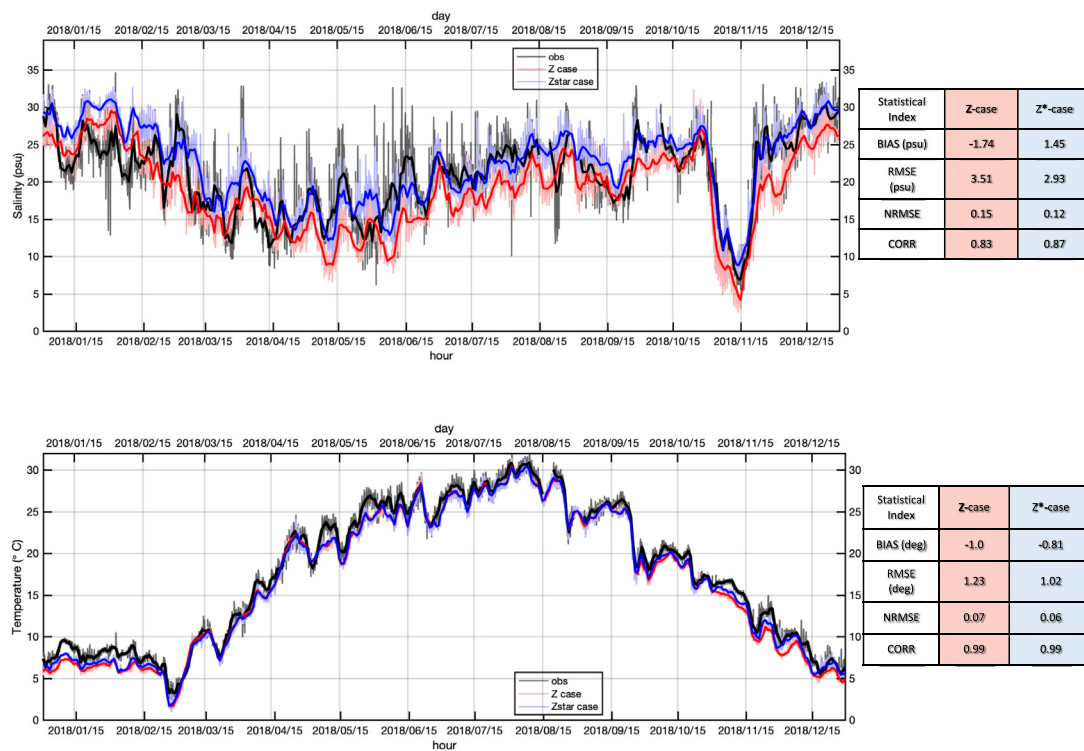
Statistical Index	Z-case	Z*-case
BIAS (psu)	-1.18	+1.20
RMSE (psu)	4.18	3.97
NRMSE	0.16	0.15
CORR	0.77	0.80

Statistical Index	Z-case	Z*-case
BIAS (deg)	-1.14	-1.12
RMSE (deg)	1.39	1.34
NRMSE	0.08	0.08
CORR	0.99	0.99

Fig. 5. Time series of simulated and observed salinity (top panel) and temperature (bottom panel) at Gorino CTD station. Shaded lines are at hourly frequency and firm lines are daily averages. The inset tables show the statistics for the z model in EXP0 and EXP2 with z^*: RMSE, BIAS, NRMSE and Pearson correlation coefficient CORR.

Statistical Index	Z-case	Z*-case
BIAS (psu)	-1.74	1.45
RMSE (psu)	3.51	2.93
NRMSE	0.15	0.12
CORR	0.83	0.87

Statistical Index	Z-case	Z*-case
BIAS (deg)	-1.0	-0.81
RMSE (deg)	1.23	1.02
NRMSE	0.07	0.06
CORR	0.99	0.99

Fig. 6. Time series of simulated and observed salinity (top panel) and temperature (bottom panel) at Mitili CTD station. Shaded lines are at hourly frequency and firm lines are daily averages. The inset tables show the statistics for the z model in EXP0 and EXP2 with z^*: RMSE, BIAS, NRMSE and Pearson correlation coefficient CORR.

stations, the bias changes sign and becomes positive, and it is still high, but slightly smaller in absolute value between z^* versus z. Overall, the RMSE and NRMSE for salinity are lower in EXP2 than EXP0, with a gain varying from 6% (Gorino station) to 30% (Venus station). We believe the comparison offered here is limited but it highlights the potential of using z^* coordinates on the coastal areas.
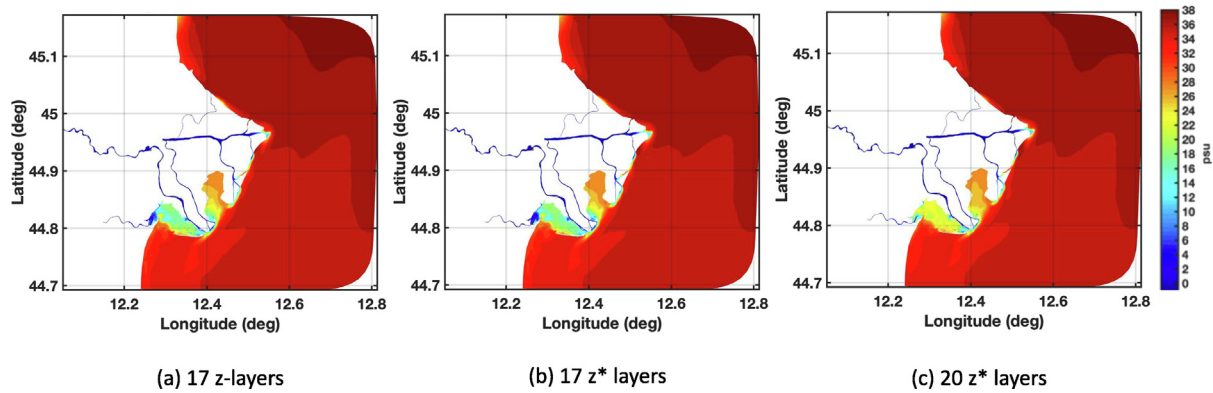
Fig. 7. Sea surface salinity during a flood tide phase with 17 layers in SHYFEM z (a), 17 layers in SHYFEM z^* (b), 20 layers in SHYFEM z^* (c) experiments.
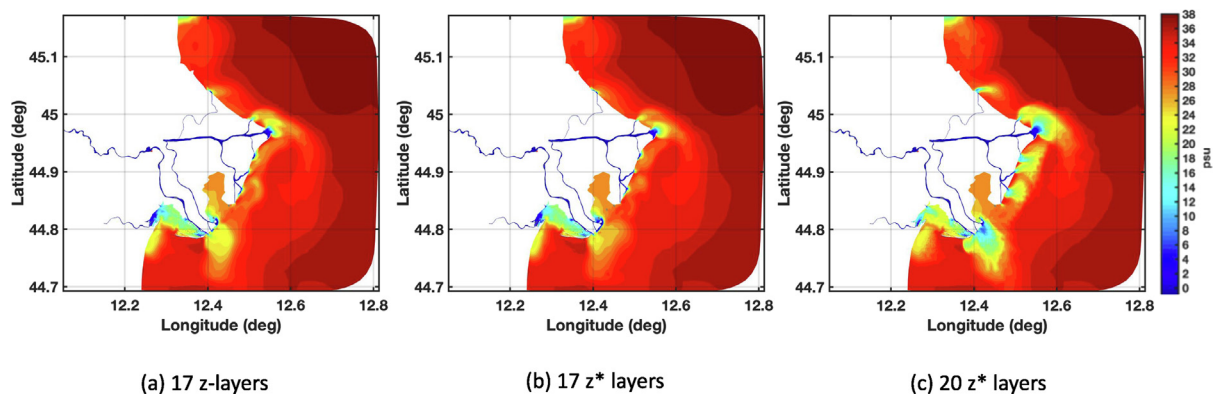

Fig. 8. Sea surface salinity during an ebb tide phase with 17 layers in SHYFEM z (a), 17 layers in SHYFEM z^* (b), 20 layers in SHYFEM z^* (c) experiments.

4.2. River plume shape and intensity

The Fig. 7 shows the sea surface salinity during a flood tide phase as simulated by the three experiments. Similarly Fig. 8 refers to the subsequent ebb tide phase. The three experiments are close to each other during the flood tide phase when the tidal current is landward oriented. However even in this phase, in the Goro lagoon the EXP2 clearly freshens the lagoon waters less near the Po di Volano mouth (dedicated discussion in Section 4.4). There are greater differences arising during the ebb tide phase by using the z^* coordinates and by increasing the number of z^* layers in the top 1 meter: the plumes of the Po river branches are better defined and offshore spreading is larger especially for EXP2 (Panel c of Fig. 8).

A transect of zonal velocity and salinity offshore the Po di Dritta mouth (Fig. 9), confirms that in the case of z^* case the freshwater plume of the Dritta branch is confined to a thinner layer and spreads further offshore with respect to the z case. We believe that this is a more faithful representation of the plume vertical structure though it is possible that other mechanisms such as the vertical mixing could be of equal importance, thus determining the realistic structure of the plume. Fig. 10 shows the profile of the gradient Richardson number, Ri, by EXP0 and EXP2 in the near-field plume, i.e. in a point selected along the same zonal transect of Fig. 9: the EXP2 shows different stratification stability values at the top ($ln(Ri) >$ – 1) and increasing stability just below the 2 m thin surface layer. EXP0 instead is less stable than EXP2 at 2 and 3 m depth and increasing in stability with depth. Overall Figs. 9 and 10 show a "bottom advected plume" versus a thin "surface advected plume" (following plume categories by Yankovsky and Chapman, 1997) in z and z^* coordinates, respectively.

4.3. River salt wedge intrusion

The Po di Goro branch is a river-dominated estuary (Valle Levinson, 2010) flowing into the micro-tidal Northern Adriatic Sea. The low tidal range makes the estuary well stratified with a salt wedge that can advance more than 20 km when moderate-to-low runoff occurs (Verri et al., 2021). We selected a 25 km thalweg along the Po di Goro branch (Fig. 11, left panel) and we compared the EXP0, EXP1 and EXP2 behavior during a flood tide phase. The right hand panel in Fig. 11 shows the profile of the gradient Richardson number Ri at the Po di Goro mouth as simulated by the 17 z-layer experiment and the 20 z^*-layer experiment: EXP2 shows a higher and more stable water column stratification corresponding to values of Ri above the critical $Ri = 0.25$ for mixing. On the other hand, EXP0 has a weaker stratification and lower Ri values. EXP2 provides an additional piece of information on the stratification of the top 1 m depth.

Fig. 12 shows the salinity transect along the Po di Goro thalweg for the selected flood tide phase. The figure highlights that working with z^* coordinates and by increasing the number of z^* layers at the top 1 meter depth, simulates a stronger intrusion of salt ocean water and the salt wedge advances a few more kilometers upstream with respect to EXP0 and EXP1. Thus the larger flexibility of the z^* model in vertical resolution near the surface leads to a stronger salt wedge intrusion with a more tilted salinity profile which is characteristic of the river-dominated estuaries.

4.4. Lagoon estuarine circulation

The Goro lagoon is characterized by an estuarine circulation (Maicu et al., 2021) with a seaward freshwater outflow in the top layer and
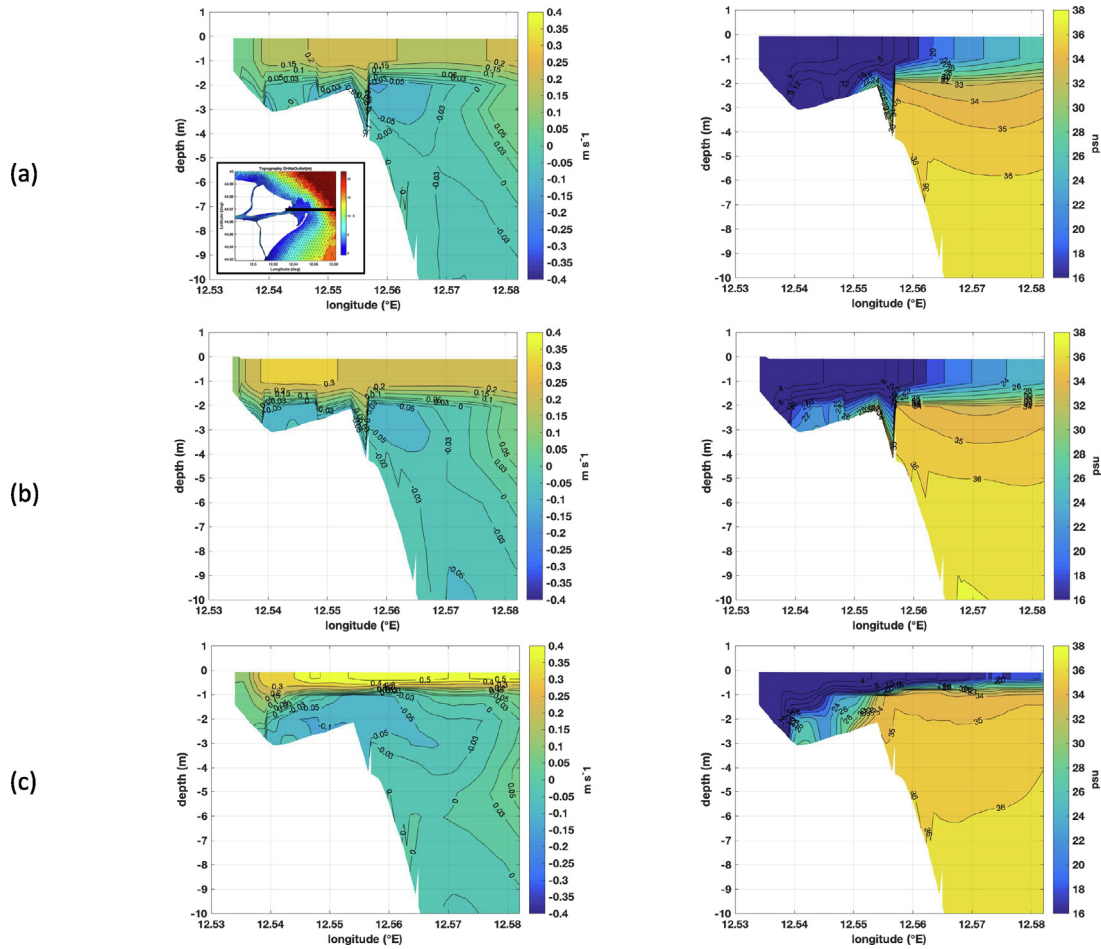
Fig. 9. Transect of zonal velocity (left) and salinity (right) from the Po di Dritta branch to the offshore during an ebb tide phase with 17 layers in SHYFEM z (a), 17 layers in SHYFEM z^* (b), 20 layers in SHYFEM z^* (c) experiments. The inset in the top-left panel shows the location of the transect (black line).
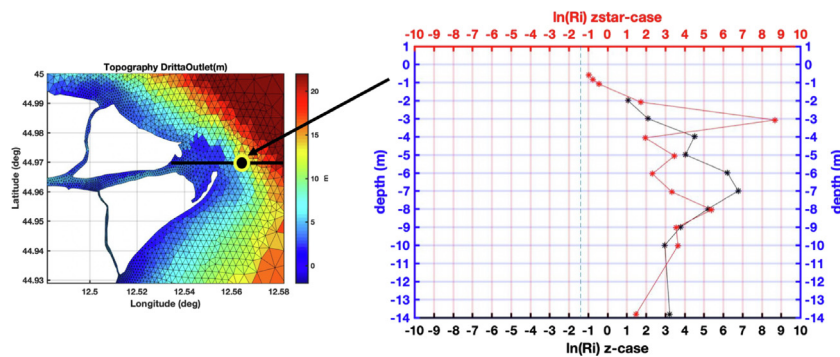

Fig. 10. Vertical profile of the logarithm of the Richardson number, $ln(Ri)$, in the near-field plume off the Po di Dritta mouth for z 17 layers (in back) and z^* 20 layers experiments (in red) during an ebb tide phase. The dashed blue line identifies the threshold value for dynamical instability, i.e. $Ri <= 0.25$.

a landward inflow of saltier water below. This circulation mechanism is connected to the inland freshwater release which includes six main sources: three channels located in the north of the lagoon, the Po di Volano branch on the western side and two narrow channels on the eastern side which connect the lagoon with the Po di Goro branch (see Fig. 3). Fig. 13 focuses on the lagoon sea surface salinity which has been averaged over 10 tidal periods (5 days) in order to exclude the effects

of the ebb–flood tides: the EXP0 and EXP1 are quite similar, while the EXP2 shows a significantly higher salinity in the inner lagoon.

We investigated the reason for this difference by comparing also the horizontal velocity at the sea surface (Fig. 14) and horizontal velocity at the sea floor (Fig. 15). EXP2 shows a faster freshwater release and slightly stronger surface currents flowing southward at the entrance of the lagoon (Fig. 14). However, the entering bottom currents which
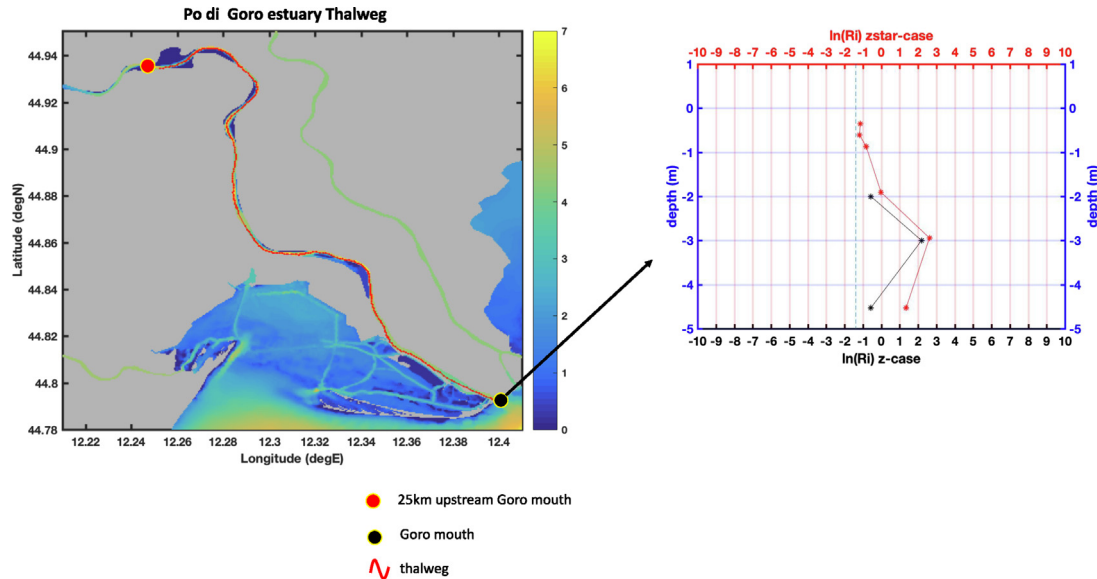
Fig. 11. Left Panel: the thalweg selected along the Po di Goro estuary. Right Panel: Vertical profile of the logarithm of the Richardson number, $ln(Ri)$, at the Po di Goro mouth for z 17 layers (in back) and z^* 20 layers experiments (in red) during a flood tide phase.
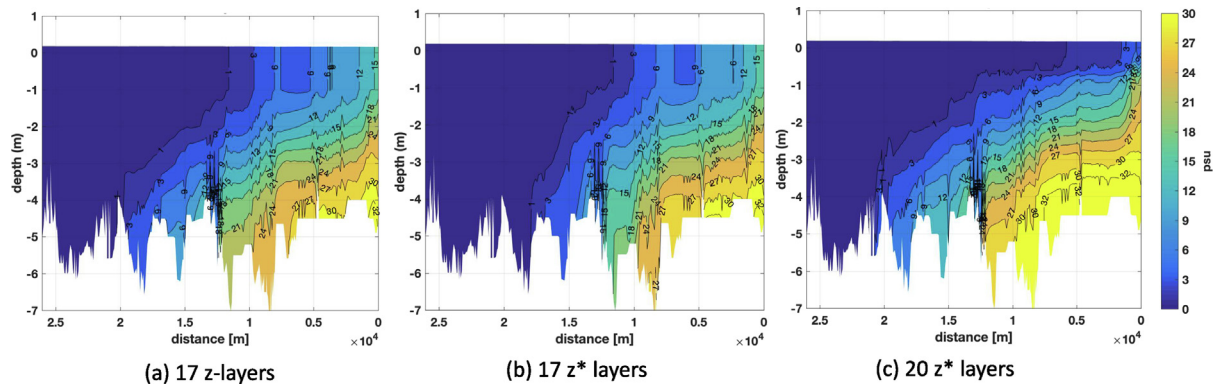

(a) 17 z-layers   (b) 17 z* layers   (c) 20 z* layers

Fig. 12. Salinity along the Po do Goro thalweg during a flood tide phase with 17 layers in SHYFEM z (a), 17 layers SHYFEM z^* (b), 20 layers in SHYFEM z^* (c) experiments.

carry salt water in the lagoon are not higher than the ones we observe in the other experiments (Fig. 15). The average subsurface inflow currents are up to 0.16 ms^{-1} in both experiments and the surface outflow is up to 0.19 ms^{-1} and 0.23 ms^{-1}, in EXP0 and EXP2 respectively. However, the net outflow at the lagoon opening is higher in EXP0 than EXP2, i.e. 52.2 m^{3}s^{-1} and 34 m^{3}s^{-1} respectively. These numbers reflect the fact that the river release is stronger but confined only in a thinner surface layer in EXP2 (as demonstrated also in Section 4.2) as result of the added stratification at the top 1 m depth. We argue this mechanism favors the upwelling of the salt water located on the shelf below the plume and the resulting higher surface salinity we observe in EXP2 (panel (c) in Fig. 13).

5. Conclusions

The present study aims at demonstrating the importance of the z^* coordinate system versus the z for the shelf slope processes, estuarine dynamics and river plumes in an unstructured grid model.

We transformed the primitive equations of the unstructured-grid, finite element and layer-integrated model SHYFEM into the z^* coordinates and we evaluated the capacity of the new model compared with the z coordinates and using available observations.

We have discussed the primitive equations in the z^* space in order to clarify their final form in a layer-integrated model and to illustrate in details the vertical boundary conditions, given that the previous literature was not sufficiently detailed.

We analyzed two cases studies in order to highlight the performance of the z and z^* coordinates in the unstructured grid model.

An initial configuration is an idealized case study already shown for structured grid models in Adcroft and Campin (2004). The case study shows the transformation of barotropic tidal motion into internal waves at the continental slope. The results of the z^*-based model shows that a higher stratification is maintained for 200 h after initialization (about 17 tidal periods) and the internal tide generation is captured better, similarly to the case reported by Adcroft and Campin (2004) for a structured model. The z coordinate model is affected by a large vertical mixing that almost prevents the internal tide generation.
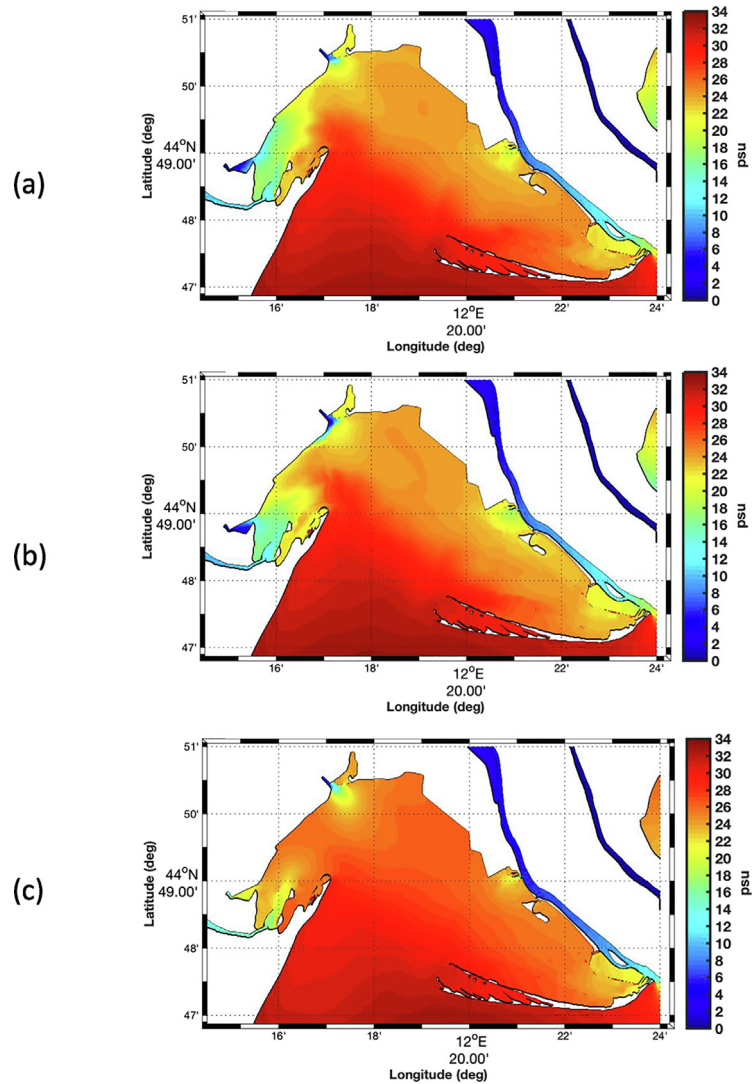
Fig. 13. Multiday averages (10 tidal periods) of Sea Surface Salinity in the Goro lagoon with 17 layers in SHYFEM z code (a), 17 layers in SHYFEM z^* code (b), 20 layers in SHYFEM z^* code (c).

The second case study considers a realistic coastal area domain and realistic atmospheric forcing. The coastal domain considered is the Po river delta system and its adjacent shelf sea. Three experiments were carried out with this configuration: two with the same number of vertical layers, one z and the other z^*, model formulations and the third with a very high resolution of the first layers which is allowed only in the z^* model formulation. Three physical processes which characterize the coastal sea dynamics were considered, the river plume shape and intensity, the estuarine water exchange with the resulting salt wedge intrusion and finally the Lagoon estuarine vertical circulation.

First we performed a detailed validation of the three model formulations for surface temperature and salinity at three CTD stations inside the lagoon. This validation shows that the z^* based code lowers the root mean square error, the normalized root mean square error and the bias for temperature while for salinity the bias changes sign, slightly decreasing in absolute value, and the root mean square and normalized root mean square errors decrease but less than for the temperature. This is likely due to the overwhelming uncertainty in the fresh water source inputs preventing the error from falling below a given threshold.

We demonstrated that the estuarine coastal sea dynamics benefits from a very fine resolution in the first meter of the water column,

i.e., 25 cm thickness layers. This high resolution in the z^* formulation model shows stronger offshore spreading of the river plumes during the ebb tide phase and a higher intrusion of salt ocean water along the Po di Goro branch at flood tide.

Overall, this study proves that the z^* together with the horizontal unstructured grid, resolving the complex geometries of river inlets and lagoons, provide a more faithful representation of the coastal sea dynamics allowing for a vertical resolution of a few tens of centimeters.

Based solely on the results presented above, we cannot state unequivocally that the z^* GVC are the most suitable coordinates system for the coastal sea dynamics. Moreover, observations from monitoring campaigns along estuaries are needed to further corroborate our results. More case studies need to be performed in the future, such as lock exchange simulations for straits and realistic bathymetry internal wave generation due to different forcings, determining the specific model vertical configuration that will allow to resolve the implied processes. A preliminary conclusion from our study is that the estuarine and the coastal sea dynamics require vertical resolutions of a few tens of centimeters at the surface, allowed by the z^* GVC, limiting the large vertical mixing that would otherwise dominate the solution.
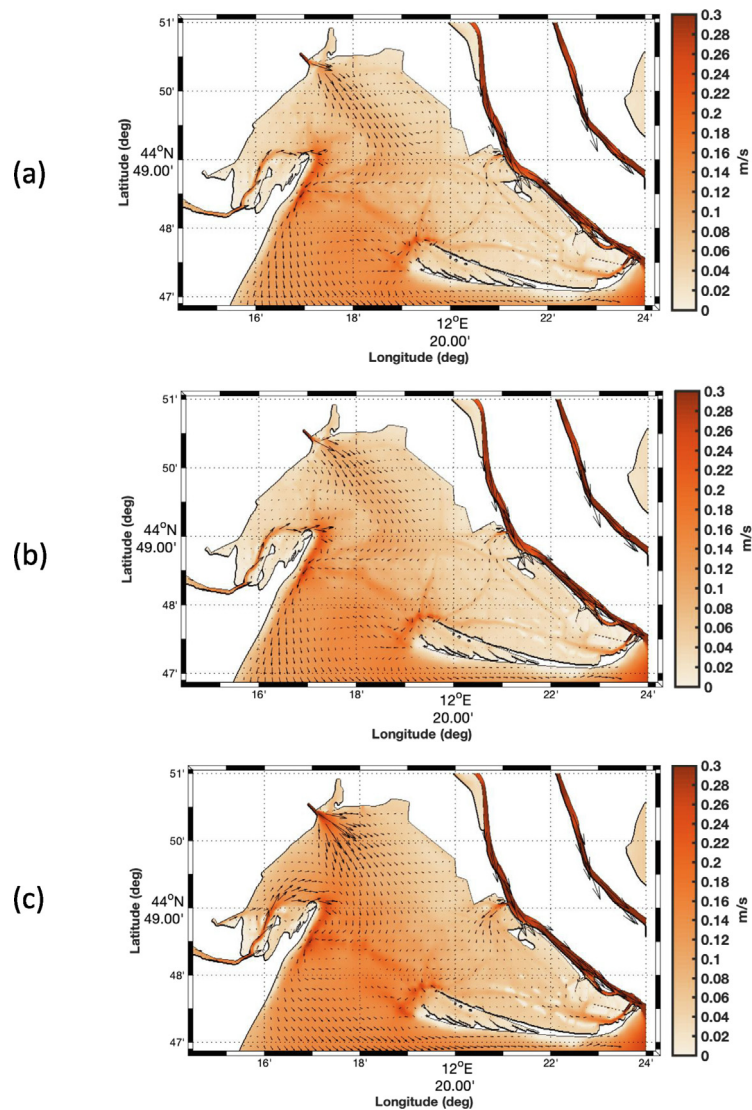
Fig. 14. Multiday averages (10 tidal periods) of horizontal velocity at the sea surface in the Goro lagoon with 17 layers in SHYFEM *z* code (a), 17 layers in SHYFEM *z** code (b), and 20 layers in SHYFEM *z** code (c).

CRediT authorship contribution statement

Giorgia Verri: Conceptualization, Methodology, Software, Visualization, Investigation, Formal analysis, Writing – original draft, Reviewing and editing. **Ivano Barletta:** Methodology, Software, Reviewing and editing. **Nadia Pinardi:** Conceptualization, Writing – original draft, Reviewing and editing. **Ivan Federico:** Resources, Validation, Reviewing and editing. **Jacopo Alessandri:** Resources, Validation, Reviewing and editing. **Giovanni Coppini:** Reviewing and editing, Funding acquiiiton.

Declaration of competing interest

The authors declare that they have no known competing financial interests or personal relationships that could have appeared to influence the work reported in this paper.

Data availability

A link is provided in the additional section "Code availability".

Code availability

The *z** version of the SHYFEM code developed and proposed in this study is available at https://doi.org/10.5281/zenodo.7773512. It is citable as Verri et al. 2023 with DOI: https://doi.org/10.5281/zenodo.7773512.
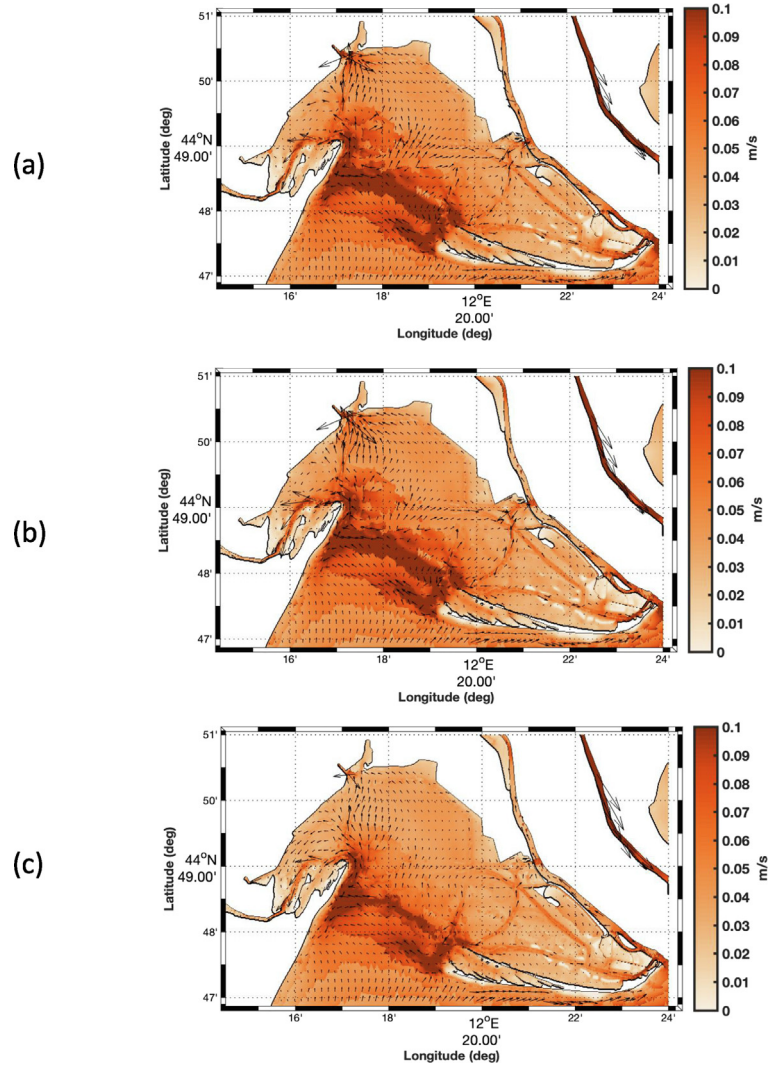
Fig. 15. Multiday averages (10 tidal periods) of horizontal velocity at the sea floor in the Goro lagoon with 17 layers in SHYFEM z code (a), 17 layers in SHYFEM z^* code (b), and 20 layers in SHYFEM z^* code (c).

Appendix. The level-discretized primitive equations in the z^* GVC

The ocean primitive equations in the z^* coordinates in "level-discretized" form are provided below. They work as a basis for comparison with the new set of SHYFEM "layer-integrated" z^* equations that we derived in this study (Eqs. (31)–(38) in Section 2.2). We wanted to re-derive the equations since in the current literature many details are lacking. The primitive equations at the z^* jth level are written:

$$\frac{\partial}{\partial t}\left(\frac{\partial z}{\partial z^*}u_j\right) + u_j\frac{\partial}{\partial x}\left(\frac{\partial z}{\partial z^*}u_j\right) + v_j\frac{\partial}{\partial y}\left(\frac{\partial z}{\partial z^*}u_j\right) + w_j^*\frac{\partial}{\partial z^*}\left(\frac{\partial z}{\partial z^*}u_j\right)$$

$$= -\frac{1}{\rho_0}\frac{\partial z}{\partial z^*}\frac{\partial p_{atm}}{\partial x} - g\frac{\partial z}{\partial z^*}\frac{\partial \eta}{\partial x} +$$

$$-\frac{g}{\rho_0}\frac{\partial z}{\partial z^*}\int_{z^*}^0\frac{\partial z}{\partial z^*}\left(\frac{\partial \rho'}{\partial x} - \frac{\partial \rho'}{\partial z}\frac{\partial z}{\partial x}\right)dz^* + \frac{\partial}{\partial z^*}(\tau_{xz_j})$$

$$+\frac{\partial z}{\partial z^*}\nabla_{h_{z^*}}\cdot(\overline{F_{u_j}^H}) - \frac{\partial z}{\partial z^*}\overline{\nabla_{h_{z^*}}(z^*)\frac{\partial F_{u_j}^H}{\partial z^*}} + \frac{\partial z}{\partial z^*}fV_j \tag{43}$$

$$\frac{\partial}{\partial t}\left(\frac{\partial z}{\partial z^*}v_j\right) + u_j\frac{\partial}{\partial x}\left(\frac{\partial z}{\partial z^*}v_j\right) + v_j\frac{\partial}{\partial y}\left(\frac{\partial z}{\partial z^*}v_j\right) + w_j^*\frac{\partial}{\partial z^*}\left(\frac{\partial z}{\partial z^*}v_j\right)$$

$$= -\frac{1}{\rho_0}\frac{\partial z}{\partial z^*}\frac{\partial p_{atm}}{\partial y} - g\frac{\partial z}{\partial z^*}\frac{\partial \eta}{\partial y} +$$

$$-\frac{g}{\rho_0}\frac{\partial z}{\partial z^*}\int_{z^*}^0\frac{\partial z}{\partial z^*}\left(\frac{\partial \rho'}{\partial y} - \frac{\partial \rho'}{\partial z}\frac{\partial z}{\partial y}\right)dz^* + \frac{\partial}{\partial z^*}(\tau_{yz_j})$$

$$+\frac{\partial z}{\partial z^*}\nabla_{h_{z^*}}\cdot(\overline{F_{v_j}^H}) - \frac{\partial z}{\partial z^*}\overline{\nabla_{h_{z^*}}(z^*)\frac{\partial F_{v_j}^H}{\partial z^*}} - \frac{\partial z}{\partial z^*}fU_j \tag{44}$$

$$\frac{\partial \eta}{\partial t} + \frac{\partial}{\partial x}\hat{U} + \frac{\partial}{\partial y}\hat{V} = P - E \tag{45}$$

$$\frac{\partial}{\partial t}\frac{\partial z}{\partial z^*} + \frac{\partial}{\partial x}\left(\frac{\partial z}{\partial z^*}u_j\right) + \frac{\partial}{\partial y}\left(\frac{\partial z}{\partial z^*}v_j\right) + \frac{\partial}{\partial z^*}\left(\frac{\partial z}{\partial z^*}w_j^*\right) = 0 \tag{46}$$

$$\frac{\partial}{\partial t}\left(\frac{\partial z}{\partial z^*}S_j\right) + \nabla_{h_{z^*}}\cdot\left(\frac{\partial z}{\partial z^*}S_j\overline{u_{j_h}}\right) + \frac{\partial}{\partial z^*}\left(\frac{\partial z}{\partial z^*}S_jw_j^*\right) =$$

$$\frac{\partial z}{\partial z^*}\nabla_{h_{z^*}}\cdot(\overline{F_{S_j}^H}) - \frac{\partial z}{\partial z^*}\overline{\nabla_{h_{z^*}}(z^*)\frac{\partial F_{S_j}^H}{\partial z^*}} + \frac{\partial}{\partial z^*}(F_{S_j}^V) \tag{47}$$

$$\frac{\partial}{\partial t}\left(\frac{\partial z}{\partial z^*}\theta_j\right) + \nabla_{h_{z^*}}\cdot\left(\frac{\partial z}{\partial z^*}\theta_j\overline{u_{j_h}}\right) + \frac{\partial}{\partial z^*}\left(\frac{\partial z}{\partial z^*}\theta_jw_j^*\right) =$$

$$\frac{\partial z}{\partial z^*}\nabla_{h_{z^*}}\cdot(\overline{F_{\theta_j}^H}) - \frac{\partial z}{\partial z^*}\overline{\nabla_{h_{z^*}}(z^*)\frac{\partial F_{\theta_j}^H}{\partial z^*}} + \frac{\partial}{\partial z^*}(F_{\theta_j}^V) + \frac{1}{\rho_0 C_p}\frac{\partial I}{\partial z^*} \tag{48}$$

$$p(x,y,z_j^*,t) = \rho_0\,gz_j^* + \int_{z_j^*}^0\frac{\partial z}{\partial z^*}\rho'g\,dz^* \tag{49}$$

$$\rho(x,y,z_j^*,t) = \rho(S_j,\theta_j,p_j) \tag{50}$$

14

where the horizontal turbulent fluxes are:

$$\overline{F^H_{u_j}} = A_H \nabla_{h_z} u_j = A_H(\nabla_{h_{z^*}} u_j + \frac{\partial z}{\partial z^*} \cancel{\nabla_{h_{z^*}}(z^*)} \frac{\partial u_j}{\partial z^*})$$

$$\overline{F^H_{v_j}} = A_H \nabla_{h_z} v_j = A_H(\nabla_{h_{z^*}} v_j + \frac{\partial z}{\partial z^*} \cancel{\nabla_{h_{z^*}}(z^*)} \frac{\partial v_j}{\partial z^*})$$

$$\overline{F^H_{S_j}} = K_H \nabla_{h_z} S_j = K_H(\nabla_{h_{z^*}} S_j + \frac{\partial z}{\partial z^*} \cancel{\nabla_{h_{z^*}}(z^*)} \frac{\partial S_j}{\partial z^*})$$

$$\overline{F^H_{\theta_j}} = K_H \nabla_{h_z} \theta_j = K_H(\nabla_{h_{z^*}} \theta_j + \frac{\partial z}{\partial z^*} \cancel{\nabla_{h_{z^*}}(z^*)} \frac{\partial \theta_j}{\partial z^*})$$

and the vertical turbulent fluxes are:

$$\tau_{xz_j} = A_V \frac{\partial u_j}{\partial z} = A_V \frac{\partial z^*}{\partial z} \frac{\partial u_j}{\partial z^*}$$

$$\tau_{yz_j} = A_V \frac{\partial v_j}{\partial z} = A_V \frac{\partial z^*}{\partial z} \frac{\partial v_j}{\partial z^*}$$

$$F^V_{S_j} = K_V \frac{\partial S_j}{\partial z} = K_V \frac{\partial z^*}{\partial z} \frac{\partial S_j}{\partial z^*}$$

$$F^V_{\theta_j} = K_V \frac{\partial \theta_j}{\partial z} = K_V \frac{\partial z^*}{\partial z} \frac{\partial \theta_j}{\partial z^*}$$

The sixth term on the right hand side of Eqs. (43) and (44) and the second terms in Eqs. (47) and (48), that are crossed, are considered negligible by most models working in GVCs (Mellor and Blumberg, 1985). This allows to highly simplify the equations even if it becomes a coarse assumption when z^* surfaces and pycnoclines are far from being aligned (Pietrzak et al., 2002).

All the partial derivatives in the equations ((43), (44), (45), (46), (47), (48) and (49)) refer to the z^* transformed space, i.e. they are: $\frac{\partial}{\partial t} = \frac{\partial}{\partial t}\big|_{z^*}, \frac{\partial}{\partial x} = \frac{\partial}{\partial x}\big|_{z^*}, \frac{\partial}{\partial y} = \frac{\partial}{\partial y}\big|_{z^*}, \frac{\partial}{\partial z^*} = \frac{\partial}{\partial z^*}\big|_{z^*}$.

The partial derivative of a scalar A with respect to c with c = (t,x,y) is:

$$\frac{\partial A}{\partial c}\big|_z = \frac{\partial A}{\partial c}\big|_{z^*} - \frac{\partial z^*}{\partial z} \frac{\partial A}{\partial z} \frac{\partial z}{\partial c}\big|_{z^*}$$

The partial derivative of a scalar A with respect to z reads:

$$\frac{\partial A}{\partial z}\big|_z = \frac{\partial z^*}{\partial z} \frac{\partial A}{\partial z^*}\big|_{z^*}$$ and the divergence of a vector $\vec{v}$ transforms as follows:

$$\nabla_z \cdot \vec{v} = \nabla_{z^*} \cdot \vec{v} - \frac{\partial z^*}{\partial z} \frac{\partial \vec{v}}{\partial z^*} \cdot \nabla_{z^*} z$$

References

Adcroft, A., Campin, J.M., 2004. Rescaled height coordinates for accurate representation of free-surface flows in ocean circulation models. Ocean Model. 7, 269–284.

Adcroft, A., Hallberg, R., 2006. On methods for solving the oceanic equations of motion in generalized vertical coordinates. Ocean Model. 11 (1-2), 224–233..

Adcroft, A., Hill, C., Marshall, J., 1997. Representation of topography by shaved cells in a height coordinate ocean model. Mon. Weather Rev. 125, 22–93.

Bellafiore, D., Umgiesser, G., 2010. Hydrodynamic coastal processes in the north Adriatic investigated with a 3D finite element model. Ocean Dyn. 60, 255–273.

Bleck, R., 1978a. Finite difference equations in generalized vertical coordinates. Part I: Total energy conservation. Contrib. Atmos. Phys. 51, 360–372.

Bleck, R., 1978b. On the use of hybrid vertical coordinates in numerical weather prediction models. Mon. Wea. Rev. 106, 1233–1244.

Bleck, R., 2002. An oceanic general circulation model framed in hybrid isopycnic-Cartesian coordinates. Ocean Model. 4, 55–88.

Bleck, R., Rooth, C., Hu, D., Smith, L., 1992. Salinity-driven thermocline transients in a wind- and thermohaline-forced isopycnic coordinate model of the North Atlantic. J. Phys. Oceanogr. 22, 1486–1505.

Blumberg, A.F., Mellor, G.L., 1987. A description of a three-dimensional coastal ocean circulation model. three-dimensional coastal ocean models. Coast. Estuar. Sci. 4, 1–16.

Bruciaferri, D., Shapiro, G., Wobus, F., 2018. A multi-envelope vertical coordinate system for numerical ocean modelling. Ocean Dyn. 68 (10), 1239–1258.

Burchard, H., Petersen, O., 1997. Hybridization between σ and z-coordinates for improving the internal pressure gradient calculation in marine models with steep bottom slopes. Internat. J. Numer. Methods Fluids 25 (9), 1003–1023.

Chiggiato, J., Paolo, O., 2008. Operational ocean models in the Adriatic Sea: A skill assessment. Ocean Sci. Discuss. 3 (6), 2087–2116.

Danilov, S., Sidorenko, D., Wang, Q., Jung, T., 2017. The finite-volume sea ice–ocean model (fesom2). Geosci. Model Dev. 10.

Egbert, G.D., Erofeeva, S.Y., 2002. Efficient inverse modeling of barotropic ocean tides. J. Atmos. Ocean. Technol. 19 (2), 183–204.

Federico, I., Pinardi, N., Coppini, G., Oddo, P., Lecci, R., Mossa, M., 2017. Coastal ocean forecasting with an unstructured grid model in the southern Adriatic and northern Ionian seas. Nat. Hazards Earth Syst. Sci. 17, 45–59.

Fofonova, V., Karna, T., Klingbeil, K., Androsov, A., Kuznetsov, I., Sidorenko, D., Danilov, S., Burchard, H., Wiltshire, K., 2021. Plume spreading test case for coastal ocean models. Geosci. Model Dev. 14.

Forget, G., Campin, J.-M., Heimbach, P., Hill, C.N., Ponte, R.M., Wunsch, C., 2015. ECCO version 4: an integrated framework for non-linear inverse modeling and global ocean state estimation. Geosci. Model Dev. 8, 3071–3104.

Griffies, S.M., 2004. Fundamentals of Ocean Climate Models, Vol. 518. Princeton University Press.

Griffies, S.M., Adcroft, A., Hallberg, R.W., 2020. A primer on the vertical Lagrangian-remap method in ocean models based on finite volume generalized vertical coordinates. J. Adv. Modelling Earth Syst. 12 (10).

Griffies, S.M., Böning, C., Bryan, F.O., Chassignet, E.P., Gerdes, R., Hasumi, H., et al., 2000. Developments in ocean climate modelling. Ocean Model. 2 (3-4), 123–192.

Hellerman, S., Rosenstein, M., 1983. Normal monthly wind stress over the world ocean with error estimates. J. Phys. Oceanogr. 13, 1093–1104.

Ilicak, M., Adcroft, A., Griffies, S., Hallberg, R., 2012. Spurious dianeutral mixing and the role of momentum closure. Ocean Model. 45, 37–58.

Jerlov, N.G., 1976. Scattering. In: Marine Optics. Elsevier Scientific Publishing Company, Amsterdam, pp. 13–22.

Kasahara, A., 1974. Various vertical coordinate systems used for numerical weather prediction. Mon. Weather Rev. 102, 509–522.

Klingbeil, K., Lemarié, F., Debreu, L., Burchard, H., 2018. The numerics of hydrostatic structured-grid coastal ocean models: State of the art and future perspectives. Ocean Model. 125, 80–105.

Leclair, M., Madec, G., 2011. Z-tilde coordinate, an arbitrary Lagrangian-Eulerian coordinate separating high and low frequency motions. Ocean Model. 37, 139–152.

Legg, S., Briegleb, B., Chang, Y., et al., 2009. Improving oceanic overflow representation in climate models: the gravity current entrainment climate process team. Bull. Am. Meteorol. Soc. 90 (5), 657–670.

Maicu, F., Alessandri, J., Pinardi, N., Verri, G., Umgiesser, G., Lovo, S., Turolla, S., Paccagnella, T., Valentini, A., 2021. Downscaling with an unstructured coastal-ocean model to the Goro Lagoon and the Po river delta branches. Front. Mar. Sci. 8.

Marshall, J., Adcroft, A., Hill, C., Perelman, L., Heisey, C., 1997. A finite-volume, incompressible Navier Stokes model for studies of the ocean on parallel computers. J. Geophys. Res. 102(C3), 5753–5766.

Mellor, G.L., Blumberg, A.F., 1985. Modeling vertical and horizontal diffusivities with the sigma coordinate system. Mon. Weather Rev. 113 (8), 1379–1383.

Mellor, G.L., Ezer, T., Oey, L., 1994. The pressure gradient conundrum of sigma coordinate ocean models. J. Atmos. Ocean. Technol. 11 (4), 1126–1134.

Mellor, G.L., Oey, L.Y., Ezer, T., 1998. Sigma coordinate pressure gradient errors and the seamount problem. J. Atmos. Ocean. Technol. 15 (5), 1122–1131.

Micaletto, G., Barletta, I., Mocavero, S., Federico, I., Epicoco, I., Verri, G., et al., 2021. Parallel implementation of the SHYFEM model. Geosci. Model Dev. Discuss. 1–33.

Oberhuber, J., 1993. Simulation of the Atlantic circulation with a coupled sea ice-mixed layer-isopycnal general circulation model. Part I: Model description. J. Phys. Oceanogr. 23 (5), 808–829.

Park, K., Federico, I., Di Lorenzo, E., Ezer, T., Cobb, K.M., Pinardi, N., Coppini, G., 2022. The contribution of hurricane remote ocean forcing to storm surge along the Southeastern US coast. Coast. Eng. 173.

Petersen, M.R., Jacobsen, D.W., Ringler, T.D., Hecht, M.W., Maltrud, M.E., 2015. Evaluation of the arbitrary Lagrangian–Eulerian vertical coordinate method in the MPAS-Ocean model. Ocean Model. 86, 93–113.

Phillips, N.A., 1957. A coordinate system having some special advantages for numerical forecasting. J. Meteorol. 14 (2), 184–185.

Pietrzak, J., Jakobson, J.B., Burchard, H., Vested, H.J., Petersen, O., 2002. A three-dimensional hydrostatic model for coastal and ocean modelling using a generalised topography following co-ordinate system. Ocean Model. 4.

Polton, J.A., Harle, J., Holt, J., Katavouta, A., Partridge, D., Jardine, J., Rousset, C., 2022. Reproducible and relocatable regional ocean modelling: fundamentals and practices. Geosci. Model Dev. Discuss. 1–47.

Ringler, T., Petersen, M., Higdon, R.L., Jacobsen, D., Jones, P.W., Maltrud, M., 2013. A multi-resolution approach to global ocean modeling. Ocean Model. 69, 2111–2232.

Russo, A., Coluccelli, A., Carniel, S., Benetazzo, A., Valentini, A., Paccagnella, T., 2013. Operational models hierarchy for short term Marine predictions: The Adriatic Sea example. MTS/IEEE OCEANS-Bergen 69, 1–6.

Shapiro, G., Luneva, M., Pickering, J., Storkey, D., 2013. The effect of various vertical discretization schemes and horizontal diffusion parameterization on the performance of a 3-D ocean model: The Black Sea case study. Ocean Sci. 9 (2), 377–390.

Shchepetkin, A., McWilliams, J., 2003. A method for computing horizontal pressure-gradient force in an oceanic model with a nonaligned vertical coordinate. J. Geophys. Res. 108, 30–90.

Song, Y., Haidvogel, D., 1994. A semi-implicit ocean circulation model using a generalized topography-following coordinate system. J. Comput. Phys. 115, 546–560.

Stacey, M., Pond, S., Nowak, Z., 1995. A numerical model of the circulation in knight inlet, British Columbia, Canada. J. Phys. Oceanogr. 25, 1037–1062.

Stelling, G.S., Van Kester, J.A.T.M., 1994. On the approximation of horizontal gradients in sigma co-ordinates for bathymetry with steep bottom slopes. Internat. J. Numer. Methods Fluids 18 (10), 915–935.

Steppeler, J., Doms, G., Schättler, U., Bitzer, H.W., Gassmann, A., Damrath, U., 2003. Meso-gamma scale forecasts using the nonhydrostatic model LM. Meteorog. Atmos. Phys. 82, 75–96.

Umgiesser, G., Canu, D.M., Cucco, A., Solidoro, C., 2004. A finite element model for the Venice Lagoon. Development, set up, calibration and validation. J. Mar. Syst. 51 (1-4), 123–145.

Valle Levinson, A., 2010. In: Valle-Levinson, A. (Ed.), Contemporary Issues in Estuarine Physics. Definition and Classification of Estuaries. Cambridge University Press, Cambridge, UK, http://dx.doi.org/10.1017/CBO9780511676567.002.

Verri, G., Mahmoudi Kurdistani, S., Coppini, G., Valentini, A., 2021. Recent advances of a box model to represent the estuarine dynamics: Time-Variable Estuary length and eddy diffusivity. J. Adv. Modelling Earth Syst. 13 (4).

von Storch, J.S., Hertwig, E., Lüschow, V., Brüggemann, N., Haak, H., Korn, P., Singh, V., 2023. Open-ocean tides simulated by ICON-O. EGUsphere 1–27.

Wise, A., Harle, J., Bruciaferri, D., O'Dea, E., Polton, J., 2022. The effect of vertical coordinates on the accuracy of a shelf sea model. Ocean Model. 170.

Yankovsky, A., Chapman, D., 1997. A simple theory for the fate of buoyant coastal discharges. J. Phys. Oceanogr. 27, 1386–1401.

Zhang, Y.J., Ateljevich, E., Yu, H.C., Wu, C.H., Jason, C.S., 2015. A new vertical coordinate system for a 3D unstructured-grid model. Ocean Model. 85, 16–21.